A Simple Model for Tidally Forced Standing Waves in a Submarine Canyon

Yuchen Ma[a,*] and **Raffaele Ferrari**[a]

[a] *Department of Earth, Atmospheric, and Planetary Sciences, Massachusetts Institute of Technology*

[*] Corresponding author: Yuchen Ma, yuchenma@mit.edu

Preprint Statement

This is a non-peer reviewed preprint submitted to EarthArXiv.

This manuscript has been submitted for peer review to the *Journal of Physical Oceanography*.

A Simple Model for Tidally Forced Standing Waves in a Submarine Canyon

Yuchen Ma,[a] Raffaele Ferrari,[a]

[a] *Department of Earth, Atmospheric, and Planetary Sciences, Massachusetts Institute of Technology*

Corresponding author: Yuchen Ma, yuchenma@mit.edu

ABSTRACT: Submarine canyons are recognized as energetic sites for internal tides and enhanced mixing, yet the mechanisms by which tidal forcing excites these motions remain poorly understood. To address this gap, we develop a simplified theoretical model that represents a canyon as a long, narrow rectangular box. The analysis reveals that the dominant wave modes in this idealized geometry are standing internal Kelvin waves, generated at the canyon-top interface by barotropic tides in the open ocean and accompanied by the radiation of internal tides back into the open ocean. The amplitude of these standing waves depends on the tidal forcing strength, the geometry-determined proximity to resonance with a given tidal frequency, and the width-to-length aspect ratio, which controls wave-radiation efficiency. Theoretical calculations indicate that the canyon's tidal kinetic energy is sustained primarily by a balance between tidal energy input and losses through radiated internal tides, with bottom drag and turbulent mixing contributing an order of magnitude less. Idealized MITgcm simulations forced by barotropic tides at the boundaries support these theoretical predictions. While the model adopts a simplified geometry, the framework can be extended to more realistic continental slope settings, providing new insight into internal tide dynamics within submarine canyons.

SIGNIFICANCE STATEMENT: While recent observations identify submarine canyons as hotspots for intense internal tides, the mechanisms governing their generation remain poorly understood. This study presents a quantitative theory using an idealized model to elucidate the dynamics of wave generation within these topographic features. These findings provide a critical theoretical foundation for future observational and modeling studies, advancing our understanding of how submarine canyons contribute to mixing and general ocean circulation.

1. Introduction

Breaking internal waves has been shown to be a dominant contributor to deep ocean mixing. These waves are often generated as the barotropic tide encounters topographic features, like seamounts and ridges, and undergo weak nonlinear interactions as they radiate away from topography until they break down into small-scale turbulence and drive mixing (e.g. Kunze 2017). More recently, submarine canyons - ubiquitous along continental margins worldwide (e.g., Allen and Durrieu de Madron 2009; Harris and Whiteway 2011)- have emerged as additional hot spots of bottom-trapped internal tides with strong shears resulting in strong local mixing rather than the remote mixing observed when waves radiate away from topography (e.g. Kunze et al. 2002; Wain et al. 2013; Alford and MacCready 2014).

Despite repeated observations of pronounced internal tides and elevated mixing within submarine canyons, a theoretical framework describing the origin of these internal tides remains sparse. Early attempts to explain internal waves in canyons as a focusing problem, initiated by Gordon and Marshall (1976) and later summarized by Hotchkiss and Wunsch (1982), relied on a ray-based description. In this viewpoint, internal waves travelling along the continental slope get trapped by multiple reflections within the steep canyon walls, ultimately concentrating near the canyon floor. Another prominent perspective stems from laboratory experiments and theoretical calculations by Baines (1983) and Grimshaw et al. (1985). These results suggest that tidal forcing can excite internal Kelvin waves within the canyon, which, upon reaching the canyon-top interface, are partially reflected back into the canyon and therefore get trapped.

Contemporary theoretical understanding of the origins of internal tides in canyons still largely depends on these earlier works. Observations, constrained by limited instrument coverage, have not supported or refuted these theoretical paradigms. Numerical simulations (e.g. Hall and Carter

2011; Zhang et al. 2014; Aslam et al. 2018; Masunaga et al. 2023) allow for a more detailed dynamical analysis, but the focus has been on the study of energy transportation indicated by internal tidal energy fluxes rather than the mechanism of internal tide excitation in confined canyon geometries.

Motivated by this gap, we analyze a theoretical model that describes the wave generation in an idealized submarine canyon at tidal frequency. Our approach is inspired by three key insights. First, the classical ray-based argument of Gordon and Marshall (1976) and Hotchkiss and Wunsch (1982) assumes that the wavelength of internal waves outside the canyon is small relative to the topographic length scale of the canyon. This assumption is questionable for internal tides. The dominant lowest-mode internal tides have wavelengths on the order of hundreds of kilometers (Zhao et al. 2016), far exceeding the typical width of submarine canyons, which generally ranges from a few hundred meters to several kilometers. Consequently, the canyon geometry strongly constrains the length scales of the waves that can survive within it, rendering a simple ray approximation invalid.

Second, numerous field studies have documented the presence of standing or partially standing wave behavior in canyon geometries rather than radiating waves (e.g., Petruncio et al. 1998; Zhao et al. 2012; Hall et al. 2017; Waterhouse et al. 2017; Alberty et al. 2017; Hamann et al. 2021; Masunaga et al. 2023), suggesting that the presence of lateral walls plays an important role in their excitation.

Third, the confined geometry of canyons has been documented to act as a resonant cavity for tidal waves both in observations (e.g.,Sutherland et al. 2005; Swart et al. 2011) and in theoretical models (e.g., Sutherland et al. 2005; Le Souëf and Allen 2014). This amplification is distinct from the effect of critical slopes, which are often emphasized in the literature on tidal-wave topography interactions.

In light of these considerations, we introduce a simplified "box-canyon" model, where the canyon is idealized as a narrow, rectangular basin with a flat bottom. The open boundary at the top is coupled with an overlying stratified ocean experiencing a tidal force. Despite omitting many real-world complexities, such as sloping or irregular boundaries, the model captures the essential physics governing the interaction between waves in the canyon and the external tidal forcing. This is discussed in the last section of the paper, where we demonstrate that the physics results in

the generation of standing patterns in the idealized canyon also apply to more realistic canyon geometries.

We conclude by illustrating how the results of the theoretical model help interpret observations from a recent field experiment that targeted a canyon in the Rockall Trough in the North Atlantic. A dye-release experiment revealed strong upwelling along the canyon axis (Wynne-Cattanach et al. 2024), apparently driven by bursts of mixing associated with intense tidal shear (Alford et al. 2025; Garabato et al. 2025). In a companion paper, Ma et al. (2025) presents a realistic simulation of the Rockall Trough canyon geometry and demonstrates the excitation of a standing-wave pattern that accounts for the observed strong tidal shear. In this paper, we provide the theoretical framework to interpret those results.

The paper is structured as follows. Sections 2 and 3 establish the theoretical foundation of the box-canyon model. Section 2 provides a summary of the principal results, while Section 3 presents the detailed mathematical derivations. Section 4 introduce the energy budget that we use to interpret the excitation of waves in the canyon. In Section 5, we compare the model predictions against a suite of idealized numerical simulations, with a focus on tidal amplitudes, phases, and energy budgets. Section 6 discusses potential adaptations and generalizations of the model to more realistic canyon geometries. Finally, Section 7 summarizes our main findings.

2. Tidal excitation of standing waves in a box-canyon: summary of the key results

In this section, we summarize the theoretical framework to investigate the excitation of internal tides in a narrow, rectangular slit carved into the ocean seafloor shown in Fig. 1, a configuration that is used as an idealized representation of a submarine canyon without a sloping bottom. This last assumption is relaxed in Section 5 where we consider a tilted domain.

For readers who wish to skip the detailed mathematical derivations that follow, we outline here the main ideas conveyed by the box-canyon model:

1. When a canyon is subject to tidal forcing, the dominant wave response at the tidal frequency consists of internal Kelvin waves. In a canyon confined between lateral walls, internal waves take the form of Kelvin and Poincaré wave modes, i.e. waves that satisfy the non-normal flow at the lateral walls. The Poincaré modes are characterized by small vertical scales are strongly damped by the strong turbulence typical of submarine canyons. As a result, the Kelvin wave

modes dominate. Furthermore, if the canyon is sufficiently narrow, these Kelvin waves can be approximated as two-dimensional wave fields, as established in previous literature (Grimshaw et al. 1985; Le Souëf and Allen 2014) and in detail below.

2. The Kelvin waves form standing modes between the end walls in the along-canyon direction, analogous to internal seiches in lakes. The gravest standing mode has an along-canyon length scale comparable to the canyon length. The standing modes result in a vertical shear pattern that alternates sign along the canyon as reported in canyon observations (Ma et al. 2025).

3. We derive the amplitudes and phases of the canyon wave modes given the amplitude and phase of the tidal forcing at the top of the canyon (either barotropic or baroclinic). The matching conditions require continuity of vertical velocity and pressure perturbations at the canyon top interface, where a three-way balance between the forcing field, the radiated wave field, and the wave field trapped inside the canyon is reached. Using these expressions, we show that the gravest canyon mode is most strongly excited when the forcing scale is much larger than the canyon width.

4. The most technically difficult part of the derivation concerns the radiated wave field, i.e., the waves scattered back into the open ocean when the forcing acts on a narrow canyon. To solve for the canyon mode amplitudes, we require a relationship between the pressure and vertical velocity of these radiated waves. However, the radiated field is a superposition of continuum of modes in (k,l,m) space, each with a different ratio of pressure to vertical velocity (an "impedance"). We show that, in the narrow-canyon limit, the net effect of all radiated modes can be represented by an effective impedance Z_R, defined as the ratio of the total radiated pressure to the total radiated vertical velocity. This effective impedance greatly simplifies both the analytical solution and the energetic discussion in the next section.

5. We identify a resonance in the canyon response, consistent with previous work of Sutherland et al. (2005) and Le Souëf and Allen (2014): when the forcing frequency matches the intrinsic modal frequency determined by the canyon geometry, the canyon wave amplitude is strongly amplified. The sharpness and magnitude of this resonance depend on a non-dimensional parameter z_n (the ratio of impedances of radiated wave modes and canyon wave modes),

which is solely controlled by the canyon aspect ratio (width relative to length). resonant modes in narrow canyons, therefore, exhibit stronger amplification than in wider ones.

3. Tidal excitation of standing waves in a box-canyon: detailed derivation

We now provide a detailed derivation of the key results summarized above.

a. Box-canyon model

The idealized canyon model is illustrated in Fig. 1 (a-c). It can be thought of as a "fish tank" carved into the seafloor. The canyon extends much farther in the along-canyon direction, L_x, than in the cross-canyon direction, L_y. At its upper boundary, the canyon is open to the overlying ocean, allowing open ocean tidal motions to interact with waves in the canyon. For simplicity, we assume that the vertical stratification N^2 is constant.

Our goal is to study how open-ocean tides excite waves in a canyon. Consistently, we assume that the waters above the canyon experience tidal waves at a single frequency, encompassing both barotropic and low-order baroclinic tides. Inspired by typical oceanographic conditions (Zhao et al. 2016; Harris and Whiteway 2011), we also assume that the open ocean tidal waves have wavelengths larger than L_x. This implies that the scale of the waves excited in the canyon is not set by the open ocean tides but rather by the canyon's geometry. This results in the generation of standing-wave patterns in the canyon, akin to seiches observed in lakes, as illustrated in Fig. 1e. A scenario that contrasts with the traditional ray-based picture depicted in Fig. 1d, where the canyon size is much larger than the open ocean tidal wavelength, so that the waves undergo multiple reflections as they propagate into the canyon.

This model geometry is chosen to capture the key features of deep ocean canyons that cut through ridges and continental shelves, such as the one sampled in the Rockall Trough experiment (Wynne-Cattanach et al. 2024). These canyons are no more than a few kilometers wide, while their lengths extend to tens of kilometers; they are subject to substantial tidal activity and experience significant turbulent mixing. All these aspects are crucial in the analysis that follows.

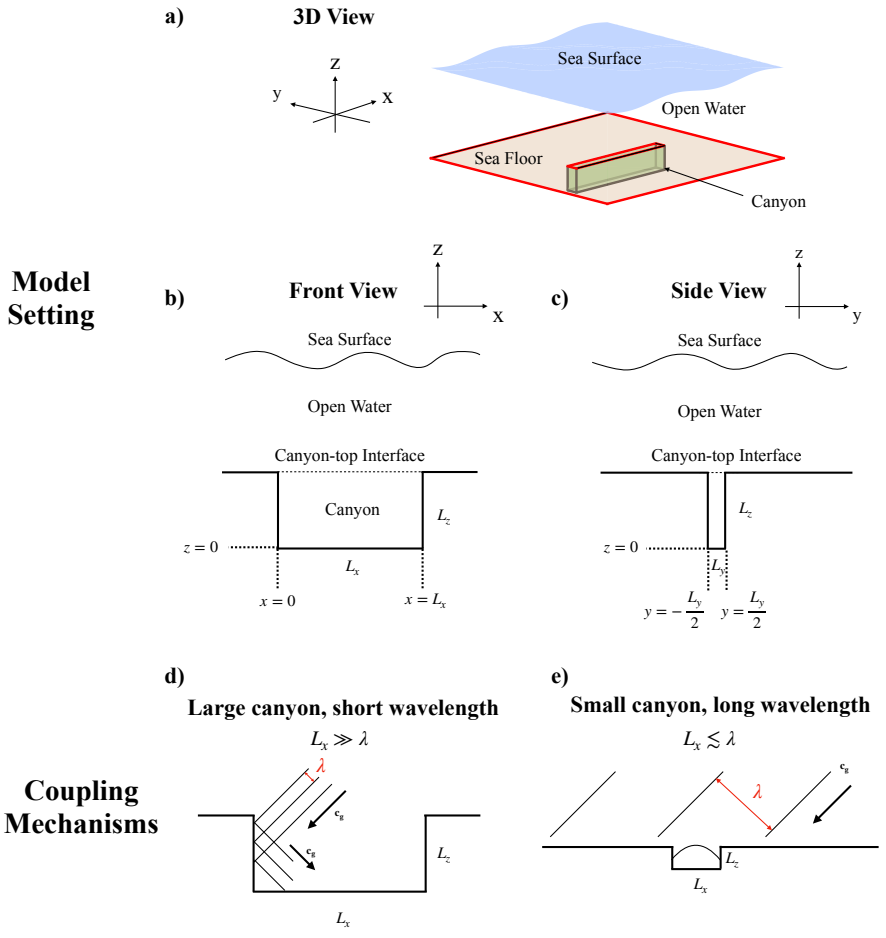

FIG. 1. (a,b,c) Settings of the box-canyon model, shown in 3D view, front and side views. The canyon has a narrow box shape with dimensions (L_x, L_y, L_z) and connects to the open ocean through a narrow slit at its top interface. (d,e) Two basic scenarios of the coupling between internal tides outside the domain and the waves inside the canyon. If the wavelength outside the canyon is much smaller than the domain sizes, then the wavelength of waves inside the canyon will be determined by waves outside the canyon. On the other hand, if the wavelength outside the canyon is comparable or larger than the domain sizes, the wavelength of modes inside the canyon would be constrained by the geometry, with the longest mode on the scale L_x. Note that the vertical scale in this sketch is exaggerated.

b. Wave modes in the box-canyon model at tidal frequency

Building on the conceptual framework described above, we now focus on the standing wave modes that can be sustained inside the canyon. To analyze these modes, we follow the conventional approach used in internal wave theory, assuming a static, stratified background state and considering small, linear perturbations to the velocity and density fields governed by the Navier–Stokes equations. We make the hydrostatic approximation, as our focus is on motions at the tidal frequency, which is much smaller than the stratification frequency N–the frequency at which vertical accelerations can no longer be neglected. Under these assumptions, the linearized governing equations take the following form:

$$\begin{cases} u_t - fv &= -p_x, \\ v_t + fu &= -p_y, \\ 0 &= -p_z + b, \\ b_t + N^2 w &= 0, \\ u_x + v_y + w_z &= 0 \end{cases} \tag{1}$$

The wave field in the canyon is constrained by the canyon bathymetry. This topographic constraint must be treated as a first-order effect. In particular, in the cross-canyon direction, the normal flow must vanish at $y = -\frac{Ly}{2}$ and $y = \frac{Ly}{2}$, resulting in a discrete set of canyon modes in y:

$$v = \sin\left(\frac{n\pi}{L_y}\left(y + \frac{L_y}{2}\right)\right), \quad n \geqslant 0 \tag{2}$$

which correspond to a Kelvin ($n = 0$) and Poincaré wave modes ($n > 0$). (While the name Poincaré waves is more commonly used to refer to surface waves in the open ocean, it is also used to refer to waves in a narrow canyon.)

The canyon modes can be determined by substituting in the system of equations (1) solutions of the form $e^{i(kx+mz-\omega t)}$ with k the along-canyon wavenumber and m the vertical wavenumber and $\omega > 0$ is the wave frequency. One obtains the dispersion relation of two classes of waves. The Poincaré wave modes satisfy

$$\frac{k^2 + (n\pi/L_y)^2}{m^2} = \frac{\omega^2 - f^2}{N^2}.$$

Typically $\omega \ll N$ for tidal waves in a stratified canyon and thus,

$$m^2 \gg k^2 + (n\pi/L_y)^2$$

The canyon's geometry has $L_x \gg L_y$ and thus k is much smaller than $n\pi/L_y$, for all but the very high n modes, and to a very good approximation $m^2 \gg \pi^2/L_y^2$. For narrow canyons a few kilometers wide–the focus of this study–this implies that the vertical wavenumber of the Poincaré modes is no more than a few hundred meters, a scale small enough to experience substantial damping in the presence of the strong background turbulent environment typically encountered in canyons. In light of this, we focus primarily on the Kelvin wave modes in the main text. A detailed analysis of the canyon's Poincaré modes, along with a demonstration of their practical irrelevance, is provided in Appendix A.

The second class of waves is in the form of Kelvin waves satisfying

$$|\frac{k}{m}| = \frac{\omega}{N} \equiv \alpha_c.$$

Kelvin waves are internal gravity waves with $v = 0$ that satisfy a reduced version of the full equations in (1):

$$\begin{cases} u_t &= -p_x \\ fu &= -p_y, \\ 0 &= -p_z + b \\ b_t + N^2 w &= 0 \\ u_x + w_z &= 0 \end{cases} \tag{3}$$

These equations represent 2D motions in the (x, z) plane supplemented by the geostrophic balance $fu = -p_y$ in the y-direction. Introducing a streamfunction ψ, such that $(u, w) = (\psi_z, -\psi_x)$ and $\psi = \hat{\psi} e^{-i\omega t}$, this system of equations can be reduced to a single equation for $\hat{\psi}$,

$$\hat{\psi}_{xx} - \alpha_c^2 \hat{\psi}_{zz} = 0, \tag{4}$$

where we relied on the assumption that N and thus α_c are constant. Solutions of this equation represent waves traveling along a wall (e.g., Rhines 1970) with the wall on their right in the northern

hemisphere. In our problem, we seek solutions confined between two lateral walls $[-L_y/2, L_y/2]$, which allows Kelvin waves to propagate in both directions, namely

$$(\psi, u, p, b) = (\psi_r, u_r, p_r, b_r)\, e^{-y/L_d + i(|k|x + mz - \omega t)} + (\psi_l, u_l, p_l, b_l)\, e^{y/L_d + i(-|k|x + mz - \omega t)}. \tag{5}$$

where $L_d \equiv \omega/(f|k|)$ is the deformation scale (e-folding scale) for the Kelvin wave with wavenumber k.

In the next few subsections, we demonstrate that the dominant waves excited in the canyon have an x-wavelength of the order of the canyon length and are much larger than the canyon width. We can thus safely assume

$$\frac{L_y}{L_d} = \frac{f|k|L_y}{\omega} \ll 1 \quad \text{consistent with} \quad |k| \ll \frac{\omega}{f}\frac{1}{L_y} \simeq \frac{1}{L_y}. \tag{6}$$

In this limit, the rightward and leftward propagating Kelvin wave solution reduces to

$$(\psi, u, p, b) \simeq (\psi_r, u_r, p_r, b_r) e^{i(|k|x + mz - \omega t)} + (\psi_l, u_l, p_l, b_l) e^{i(-|k|x + mz - \omega t)}. \tag{7}$$

where the y-dependence is weak because $y < L_y \ll L_d$ as long as $e^{y/L_d} \sim 1$ and can thus be neglected at leading order, except when taking y-derivatives of pressure. The y-pressure gradient enters at leading order and balances the Coriolis acceleration, $fu = -p_y$. An additional approximation pertains to the non-normal flow boundary condition at the edges of the canyon at $x = 0$ or $x = L_x$, which in general requires a combination of Kelvin and Poincaré modes. However, in the limit of a narrow canyon ($L_y \ll L_d$), Taylor (1922) [1] shows that the incoming Kelvin wave reflects off the wall with a phase difference of approximately π and minimal excitation of Poincaré waves, and thus the reflection problem is essentially two-dimensional. In a narrow channel, we can therefore safely neglect the y-dependence at leading order and treat the solution as effectively two-dimensional. In practice, we replace the full streamfunction $\psi(x, y, z, t)$ by the 2D field $\psi(x, z, t) \equiv \psi(x, y = 0, z, t)$ at the centerline and approximate the boundary condition as $\psi = \psi_l + \psi_r = 0$ at $x = 0$ and $x = L_x$ as in a 2D wave–reflection problem.

[1] Taylor (1922) solves the problem for surface Kelvin and Poincaré in a canyon rather than the internal wave problem considered here, but the analysis is equivalent.

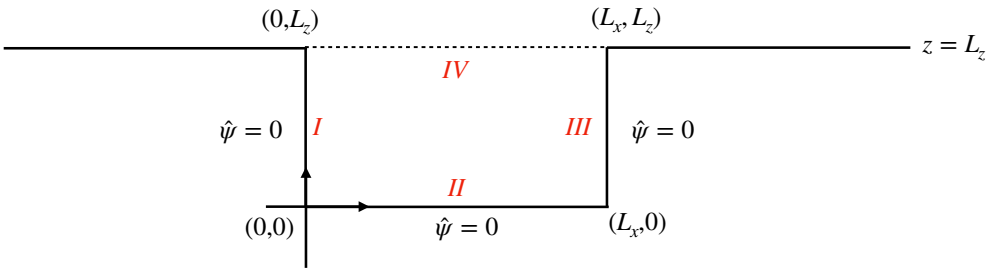

FIG. 2. Boundary condition for standing internal Kelvin wave modes in the canyon.

Without y-dependence, solutions to Eq. (4) can be written as $\psi = \hat{\psi}(x,z)e^{-i\omega t}$, with $\hat{\psi}(x,z)$ a complex amplitude to be determined by supplementing boundary conditions. With the domain depicted in Fig. 2, $\hat{\psi}$ must be set to zero along the rigid walls I, II, and III. The boundary condition at the interface IV is set by matching the Kelvin wave solution with the motions in the overlying ocean and is discussed in detail later in this section. Solutions satisfying Eq. (4) and the three boundary conditions at the rigid walls can be written as the sum of discretized normal modes:

$$\hat{\psi}_{CA} = \sum_{n=1}^{\infty} \tilde{A}_n \hat{\psi}_n, \quad \text{with} \quad \hat{\psi}_n(x,z) = \sin(k_n x)\sin(m_n z) \tag{8}$$

where

$$k_n = \frac{n\pi}{L_x}, \quad m_n = \frac{k_n}{\alpha_c} = \frac{1}{\alpha_c}\frac{n\pi}{L_x}, \quad n \geqslant 1 \tag{9}$$

The lateral boundaries discretize the wavenumber k_n, while the wavenumber m_n is determined by the governing equation (4) and the associated Kelvin wave dispersion relation. $\tilde{A}_n$ are the complex amplitudes encapsulating both amplitude and phases of mode n (in what follows, the tilde sign

always carry the meaning of complex amplitude). The corresponding solutions for $\hat{u}, \hat{w}, \hat{b}, \hat{p}$ are

$$\begin{cases} \hat{u}_{\mathrm{CA}}(x,z) & = \sum_n \tilde{A}_{un}\hat{u}_n(x,z) = \sum_n m_n \tilde{A}_n \sin(k_n x)\cos(m_n z) \\ \hat{w}_{\mathrm{CA}}(x,z) & = \sum_n \tilde{A}_{wn}\hat{w}_n(x,z) = \sum_n -k_n \tilde{A}_n \cos(k_n x)\sin(m_n z) \\ \hat{b}_{\mathrm{CA}}(x,z) & = \sum_n \tilde{A}_{bn}\hat{b}_n(x,z) = \sum_n -\frac{iN^2}{\omega} k_n \tilde{A}_n \cos(k_n x)\sin(m_n z) \\ \hat{p}_{\mathrm{CA}}(x,z) & = \sum_n \tilde{A}_{pn}\hat{p}_n(x,z) = \sum_n \frac{-i\omega}{\alpha_c} \tilde{A}_n \cos(k_n x)\cos(m_n z) \end{cases} \tag{10}$$

Fig. 3 illustrates the first three normal modes for a representative rectangular box. The aspect ratio of the modal cells is governed by the constant α_c. While the spatial patterns of these modes are unaffected by the upper boundary condition at boundary IV, their amplitudes are set by it, as discussed below.

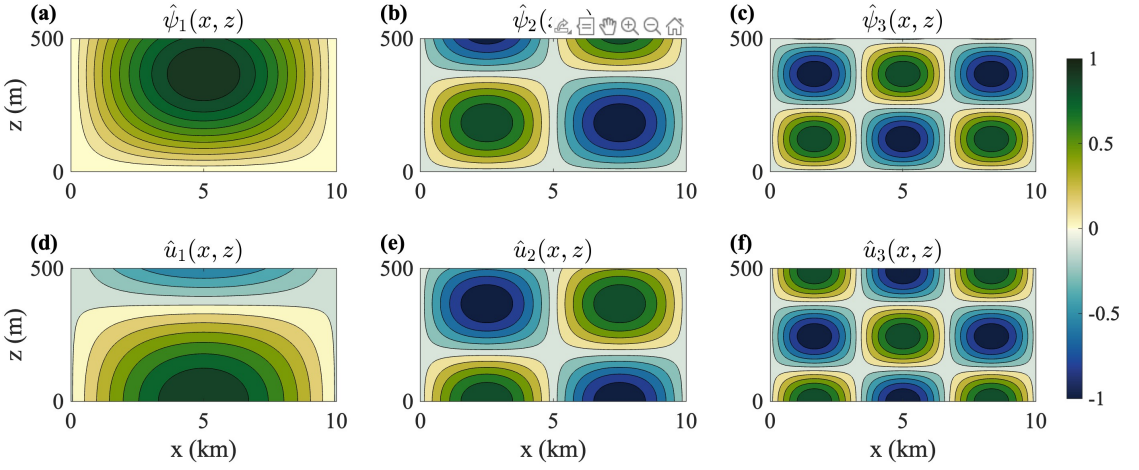

FIG. 3. Streamfunction and along-canyon velocity of the first three modes in the box-canyon model, with $L_x = 10$km, $L_z = 500$ m, $\alpha_c = 0.073$ (patterns not sensitive to these values).

c. Tidal forcing outside the canyon

Tidal motions in the open ocean consist of both barotropic and baroclinic components. Accordingly, we represent the motions above the canyon as the superposition of a barotropic tidal wave, expressed in terms of the sea surface displacement η, and horizontally propagating baroclinic waves that satisfy a no-normal-flow condition at the ocean surface and bottom. We focus on the

lowest-order baroclinic waves, as they generally carry the majority of the total baroclinic tidal energy.

The wave solutions within the canyon must match the tidal flow outside at the upper interface, located at $z = L_z$ and spanning the narrow strip $[0, L_x] \times [-L_y/2, L_y/2]$. Because the dominant tidal motions in the open ocean have horizontal scales far exceeding the canyon width, we neglect their y-variation when applying the boundary conditions at the canyon top, i.e.,

$$\hat{p}_F(x) = \hat{p}_F(x, y = 0, z = L_y) = g\tilde{\eta}_0 e^{iK_0 x} + \tilde{p}_1' e^{iK_1 x}, \qquad \text{with } p_F(x) = \hat{p}_F(x) e^{-i\omega t} \tag{11}$$

where K_0 and K_1 are the wavevector components of the barotropic tide and lowest baroclinic tide along the canyon axis–x in our notation.

To impose the boundary condition at the interface, we start by projecting the open ocean tidal wave onto the basis functions of the canyon modes shown in (10). The canyon pressure field is expressed as a function of a discrete set of cosine modes $\cos(k_n x)$, with $k_n = n\pi/L_x$. This set forms a complete and orthogonal basis on $[0, L_x]$ and we can therefore represent $\hat{p}_F(x)$ in terms of these basis functions:

$$\hat{p}_F(x) = \tilde{C}_0 + \sum_{n=1}^{N} \tilde{C}_n \cos(k_n x) \tag{12}$$

Here, $\tilde{C}_n$ represents the complex amplitude of the n-th mode induced by the forcing, truncating at order N. The term $\tilde{C}_0$ corresponds to a spatially uniform component that does not influence the flow and can therefore be neglected.

To gain some insight on the dependence of the coefficients $\tilde{C}_n$ with modal number n, we consider the limit where the length of the canyon, in addition to its width, is much shorter than the scale of the tidal waves in the ocean interior, i.e. $K_0 L_x \ll K_1 L_x \ll 1$, which applies well to relative shorter canyons of 10-20 km. In this limit, we can represent the pressure as a linear gradient in x over the distance L_x (a Taylor series expansion of the pressure profile that retains only the constant and linear terms in x):

$$\begin{aligned} \hat{p}_F(x) &\approx \hat{p}^F_{x0} x + \hat{p}^F_0 \\ &= -\hat{p}^F_{x0} \sum_{n \text{ is odd}} \frac{4L_x}{n^2\pi^2} \cos(k_n x) + \hat{p}^F_0 \end{aligned} \tag{13}$$

where $\hat{p}^F_{x0} = \left.\frac{\partial \hat{p}^F}{\partial x}\right|_{x=0}$ is the pressure gradient at $x = 0$ and $-\sum_{\text{odd}} 4L_x/(n^2\pi^2)\cos(k_n x)$ is the Fourier representation of x under $\{\cos(k_n x)\}$ bases. This is the well-known result that a function with different values at the edge of the domain at $x = 0$ and $x = L_x$ has Fourier coefficients $\tilde{C}_n$ that decay as n^2. This suggests that the external tidal forcing most strongly excites low-order odd modes in the canyon. If the pressure fields varies more smoothly than a step function at the edge of the domain, i.e. if the canyon length is comparable to the tidal wave wavelength, then the spectral roll-off is even steeper.

d. Radiated waves outside the canyon

The standing waves in the canyon trigger pressure and velocity perturbations at the interface, which radiate up above the open ocean. The radiated waves induced by canyon wave modes have been extensively examined by Grimshaw et al. (1985), who employed a Green's function approach. In their formulation, the vertical velocity field is treated as a distribution of individual wave sources, and the resulting radiated pressure field at the canyon top is computed in physical space. We find that spectral characterization is more informative if formally equivalent.

Specifically, the radiated waves form an internal wave field comprising all wavenumber triplets (k, l, m) that satisfy the dispersion relation

$$\frac{\sqrt{k^2 + l^2}}{-m} = \frac{\sqrt{\omega^2 - f^2}}{N},$$

where $m < 0$ because waves radiated from the canyon propagate upward. For each mode, the pressure amplitude and vertical velocity are related through the concept of impedance (e.g., Gill 2016), defined as the ratio of pressure to vertical velocity. This relationship follows directly from the third and fourth equations in the governing system (1):

$$Z(k, l) \equiv \frac{\hat{p}}{\hat{w}} = -\frac{N^2}{m\omega} = \frac{N}{\sqrt{k^2 + l^2}} \frac{\sqrt{\omega^2 - f^2}}{\omega}. \tag{14}$$

Applying this impedance relation allows us to write the pressure field to be written based on the vertical velocity field for the radiated waves:

$$\begin{aligned}\hat{w}_R(x,y,z\geqslant L_z) &= \int_{-\infty}^{\infty}\int_{-\infty}^{\infty} \hat{w}_R(k,l)\, e^{i(kx+ly+m(z-L_z))}\, dk\, dl,\\ \hat{p}_R(x,y,z\geqslant L_z) &= \int_{-\infty}^{\infty}\int_{-\infty}^{\infty} Z(k,l)\,\hat{w}_R(k,l)\, e^{i(kx+ly+m(z-L_z))}\, dk\, dl,\end{aligned} \tag{15}$$

where m is determined by (k,l) through the dispersion relation and $\hat{w}_R(k,l)$ is the vertical velocity amplitude for the wavenumber pair (k,l). Since our focus is on the coupling between fields at the canyon interface, we neglect y-variations in the radiated waves (see Appendix B) and project the radiated field at the interface onto the basis functions of the canyon modes, truncating at order N:

$$\begin{aligned}\hat{w}_R(x,y=0,z=L_z) &= \sum_{n=1}^{N} \tilde{B}_{wn}\cos(k_n x),\\ \hat{p}_R(x,y=0,z=L_z) &= \sum_{n=1}^{N} \tilde{B}_{pn}\cos(k_n x).\end{aligned} \tag{16}$$

To facilitate the discussion of mode coupling, we seek a relationship between $\tilde{B}_{pn}$ and $\tilde{B}_{wn}$, which can be interpreted as the effective impedance in the modal basis. In general, this effective impedance forms an $N\times N$ tensor, whose elements represent the ratio of every possible combination of pressure and velocity modes. For a narrow canyon ($L_y \ll L_x$), however, numerical evaluation shows that the tensor is strongly dominated by its diagonal elements. To a good approximation,

$$\tilde{B}_{pn} \simeq Z_R(k_n)\,\tilde{B}_{wn}, \tag{17}$$

which is equivalent to the "plane-wave approximation" of Grimshaw et al. (1985), and Z_R can be approximated by

$$Z_R(k_n) \simeq \frac{N}{k_n}\frac{\sqrt{\omega^2-f^2}}{\omega}\frac{1}{2\pi}\left[-\ln(k_n L_y)\,k_n L_y + O(k_n L_y)\right]. \tag{18}$$

The derivation is given in Appendix B.

Two observations help interpret the behaviour of Z_R: (i) The prefactor in (18), namely $\frac{N}{k_n}\frac{\sqrt{\omega^2-f^2}}{\omega}$, is inherited from the plane-wave impedance (14). (ii) As $L_y \to 0$, $Z_R \to 0^+$, so that for fixed canyon

length, a narrower canyon always leads to smaller effective impedance. Physically, for a given k, modes with larger l have smaller impedance according to (14). The effective impedance Z_R represents an average impedance over all admissible l modes. A narrower canyon (smaller L_y) shifts the spectrum toward larger l and therefore reduces the overall average impedance.

e. Coupling of wave fields at the canyon-top interface

Armed with the modal basis and the scale analysis of open-ocean tidal waves, we now implement the boundary condition at the canyon-top interface (boundary *IV* in Fig. 2) to determine the amplitudes and phases of the standing waves excited within the canyon. At this interface, the pressure and vertical velocity fields in the canyon, $(\hat{w}_{\mathrm{CA}}, \hat{p}_{\mathrm{CA}})$, must satisfy the continuity conditions:

$$\begin{cases} \hat{p}_{\mathrm{CA}}(x, z = L_z) = \hat{p}_F(x) + \hat{p}_R(x, z = L_z), \\ \hat{w}_{\mathrm{CA}}(x, z = L_z) = \hat{w}_R(x, z = L_z), \end{cases} \tag{19}$$

where $\hat{p}_F$ is the open-ocean forcing pressure at the interface, and $\hat{p}_R$ and $\hat{w}_R$ are the pressure and vertical velocity fields of waves radiated out of the canyon, as introduced earlier. There is no vertical velocity $\hat{w}_F$, because the barotropic tidal motions have no vertical velocity by definition and the low order baroclinic tidal wave vertical velocity is zero on both sides of the canyon at $z = L_z$ to satisfy the no-normal flow condition and must therefore be zero over the canyon as well if their scales are much larger than the canyon width.

We substitute the modal expansions for each field at the interface (10), (12), and (16) into the boundary conditions (19) and combine them with the impedance relationships for the canyon waves (10) and for the radiated waves (17). This yields the following system of four equations for the four unknowns $(\tilde{A}_{pn}, \tilde{A}_{wn}, \tilde{B}_{pn}, \tilde{B}_{wn})$:

$$\begin{cases} \tilde{A}_{pn} \cos(m_n L_z) = \tilde{C}_n + \tilde{B}_{pn}, \\ \tilde{A}_{wn} \sin(m_n L_z) = \tilde{B}_{wn}, \\ \tilde{A}_{pn} = i \frac{N}{k_n} \tilde{A}_{wn}, \\ \tilde{B}_{pn} \simeq Z_R(k_n)\, \tilde{B}_{wn}. \end{cases} \tag{20}$$

Solving this system for $\tilde{A}_{pn}$ gives

$$\tilde{A}_{pn} = \frac{\tilde{C}_n}{\cos(m_n L_z) + i\, Z_R(k_n)\, \frac{k_n}{N} \sin(m_n L_z)} = \frac{\tilde{C}_n}{\cos(m_n L_z) + i\, z_n \sin(m_n L_z)}, \tag{21}$$

Once $\tilde{A}_{pn}$ is determined from (21), the amplitudes of the remaining canyon field components follow directly from the relationships for the canyon wave fields given in (10).

In (21), we introduced

$$\begin{aligned} z_n &\equiv Z_R(k_n)\, \frac{k_n}{N} \\ &= \frac{\sqrt{\omega^2 - f^2}}{\omega}\, \frac{1}{2\pi} \left[-k_n L_y \ln(k_n L_y) + O(k_n L_y) \right], \end{aligned} \tag{22}$$

as the nondimensional ratio between the impedance of the radiated wave, $Z_R(k_n)$, and the impedance of a standing wave in the canyon, given by $|\tilde{A}_{pn}/\tilde{A}_{wn}| = N/k_n$. Given the continuity of vertical velocity between the radiated and canyon waves at the interface (19), the parameter z_n quantifies the pressure amplitude of the radiated wave relative to that of the canyon wave, and thus controls the fraction of the canyon's energy flux that can escape into the open ocean. A detailed discussion of the corresponding energy budget is presented in the next section. Since $k_n = n\pi/L_x$, (22) indicates that z_n is determined solely by the canyon aspect ratio L_y/L_x and the frequency ratio f/ω. Fig. 4 presents z_n for modes 1, 3, and 5 of the Kelvin-wave mode; even modes are omitted because they are much more weakly forced, as discussed previously. For all modes, z_n decreases with canyon narrowing and increases with canyon widening, consistent with the trend of Z_R we discussed previously. In addition, lower-order modes have consistently smaller impedance ratios.

As $z_n \ll 1$ for narrow canyons, the cosine term in (21) primarily controls the amplification of the canyon pressure field. For the most strongly forced lowest-order mode (mode 1), tidal resonance occurs when $m_1 L_z = (2n+1)\,\pi/2$, or equivalently $2L_z/L_x = (2n+1)\,\alpha_c$. At resonance, the peak amplitude of the canyon pressure response is set mainly by z_n and scales as $\tilde{C}_n/z_n$. This behavior is analogous to earlier resonance-fitting models (e.g., Sutherland et al. 2005; Le Souëf and Allen 2014), where the damping strength determined the resonant amplitude; however, in those studies the dominant damping was attributed to bottom friction, whereas here we argue that energy leakage is the more significant mechanism. The details of this energy-budget analysis, including

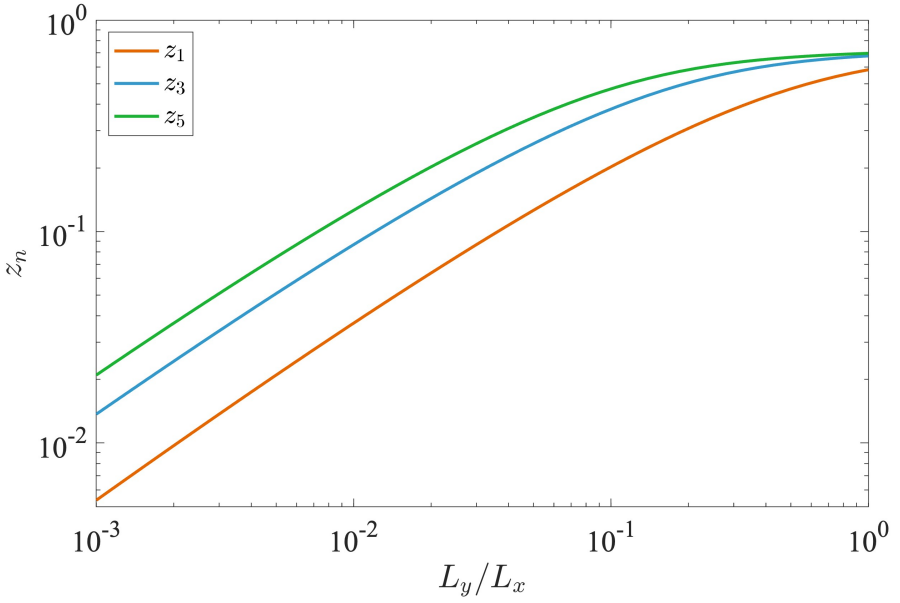

FIG. 4. Impedance ratio z_n plotted as a function of the aspect ratio L_y/L_x for modes 1, 3, and 5. The results are shown for a representative case with $f = 1\times10^{-4}$ s^{-1} and the M2 tidal frequency $\omega \simeq 1.45\times10^{-4}$ s^{-1}.

a comparison of the relative strengths of the two energy-extraction processes, are presented in the next section.

4. Energy budget in the box-canyon system

a. Energy budget of the linear wave system

Our box-canyon model provides a solution for the wave fields in the canyon subject to a tidal forcing applied at the canyon-top interface. We analyze its energy budget to see the dominant energy source and sink of this equilibrium system in this section.

The evolution of the horizontal kinetic energy density, $E_k \equiv \frac{1}{2}u^2$, and the potential energy density, $E_p \equiv \frac{1}{2}\frac{b^2}{N^2}$ (ρ_0 factor omitted for simplicity), under the governing wave Eq. (3) can be derived as:

$$\begin{cases} \dfrac{\partial E_k}{\partial t} = -\nabla\cdot(\mathbf{u}p) + bw, \\ \dfrac{\partial E_p}{\partial t} = -bw. \end{cases} \tag{23}$$

To understand the energy budget averaged over the entire canyon system, we compute the volume average of the above equations. This yields:

$$\begin{cases} \dfrac{\partial \overline{E_k}^{x,z}}{\partial t} = -\dfrac{1}{L_z}\overline{w\,p}^{x}\Big|_{z=L_z} + \overline{b\,w}^{x,z}, \\ \dfrac{\partial \overline{E_p}^{x,z}}{\partial t} = -\overline{b\,w}^{x,z}. \end{cases} \tag{24}$$

Here, $\overline{\cdot}^{x,z}$ denotes the volume average over the canyon, and the $\overline{\cdot}^{x}|_{z=L_z}$ denotes the x-average over the canyon-top interface at $z = L_z$. Since the wave system is in equilibrium and we are not including any energy dissipation at this stage, the net tendency terms vanish if averaged over a tidal cycle. We thus have $\overline{b\,w}^{x,z,t} = \frac{1}{L_z}\overline{w\,p}^{x,t}\big|_{z=L_z} = 0$, where $\overline{\cdot}^{t}$ represents time average over a tidal cycle.

We can further decompose the total energy flux into a forcing term by recognizing that at the canyon-top interface the pressure and vertical velocity can be written as $p = p_F + p_R$ and $w = w_R$ as we have discussed in Eq. (19), and thus:

$$0 = \overline{w_R\,p_F}^{x,t}\Big|_{z=L_z} + \overline{w_R\,p_R}^{x,t}\Big|_{z=L_z}. \tag{25}$$

With this decomposition $\overline{w_R\,p_F}^{x,t}\big|_{z=L_z} < 0$ represents the energy injected into the system by the forcing, while $\overline{w_R\,p_R}^{x,t}\big|_{z=L_z} > 0$ corresponds to the energy that leaks out of the system via radiated waves.

The energy leaking out of the system can be directly computed from our solutions presented in the previous section. Specifically, we have:

$$-\overline{w_R\,p_F}^{x,t}\Big|_{z=L_z} = \overline{w_R\,p_R}^{x,t}\Big|_{z=L_z} \simeq \frac{1}{4}\sum_n |\tilde{B}_{wn}|^2\, Z_R(k_n) = \frac{1}{4}\sum_n |\tilde{A}_{wn}|^2 \sin^2(m_n L_z)\, Z_R(k_n), \tag{26}$$

where we have used the relation in (20) in above derivations.

From the above expressions, we see that energy leakage is governed by two factors: the effective impedance Z_R and the proximity of the system to resonance which strongly influences $\sin(m_n L_z)$. The effective impedance of the radiated waves Z_R increases with canyon width as shown in (18). Consequently, leakage is more pronounced in wider canyons, in agreement with common intuition

and the analysis by Grimshaw et al. (1985). Additionally, leakage is enhanced when the system is near resonance (e.g., when $m_1 L_z \sim n\pi/2$ for the most energetic mode), since stronger vertical motions are generated at the canyon-top interface, thereby radiating more energy outward.

In the limiting case of a very narrow canyon, where Z_R is small, little energy leaks out of the system. Under these conditions, the pressure forcing performs minimal work on the system. As seen from (21), when $Z_R \sim 0$, the phase lag between the forcing and the pressure response in the canyon is either 0 or π. Since the vertical motion lags the pressure response (and hence the forcing) by $\pi/2$, no net work is done over a tidal cycle, resulting in no net energy input into the system.

b. Other energy extraction mechanisms

The formulae derived in the previous sections assumed that the entire system is governed solely by the wave dynamics, thereby neglecting the effects of bottom friction and turbulent dissipation. In reality, these processes can also extract energy from the system, especially the fact that the bottom drag has been hypothesized as the dominant damping mechanism in previous tidal resonance models (e.g., Sutherland et al. 2005; Le Souëf and Allen 2014).

For the sake of only a scale comparison, we assume a linear drag law given by$\tau = -\rho_0 C_L u$ for simplicity, and the work done by the bottom drag at the bottom interface $z = 0$ would be given by

$$\overline{\tau u}^{x,t}\big|_{z=0} = -\rho_0 C_L \overline{u^2}^{x,t}\big|_{z=0} = -\rho_0 C_L \frac{1}{4}\sum_n |\tilde{A}_{un}|^2 = -\rho_0 \frac{N^2}{\omega^2} C_L \frac{1}{4}\sum_n |\tilde{A}_{wn}|^2, \tag{27}$$

where we have used the relation $|\tilde{A}_{un}|^2 = N^2/\omega^2 |\tilde{A}_{wn}|^2$ in (10) to convert the horizontal velocity amplitude to the vertical velocity amplitude to be consistent with (26).

We can now estimate the ratio of energy extraction due to leakage through the canyon top (via the radiated wave) to that due to bottom drag. For the first mode, this ratio is

$$\frac{\rho_0 \frac{1}{L_z}\overline{w_R p_R}\big|_{z=L_z}}{\frac{1}{L_z}\left|\overline{\tau u}\big|_{z=0}\right|} \approx \frac{\sin^2(m_1 L_z)\,\frac{N^2}{m_1\omega} z_1}{\frac{N^2}{\omega^2} C_L} = \sin^2(m_1 L_z)\, z_1 \frac{\omega}{m_1}\frac{1}{C_L}. \tag{28}$$

Here, ω/m_1 is the vertical phase speed of the lowest-order Kelvin wave, which is approximately $\omega/m_1 \approx 0.03$ m s^{-1} for M2 tidal frequency with $N^2 = 4\times10^{-6}$ s^{-2} and $L_x \sim 10$ km. For a typical canyon aspect ratio of 0.1, Fig. 4 gives $z_1 \approx 0.1$. Assuming a linear drag coefficient

$C_L \approx 10^{-4}$ m s^{-1} for tidal velocities of $O(0.1)$ m s^{-1}, we obtain $z_n\omega/(m_1 C_L) \approx 30$. Thus, as long as $\sin^2(m_1 L_z) \gtrsim O(0.033)$, leakage dominates the total energy extraction. Only in the special case where $\sin(m_1 L_z) \approx 0$, the vertical velocity at the interface (10) vanishes and no energy is radiated into the open ocean, leaving bottom drag as the sole dominant extraction mechanism.

A similar estimation shows that the energy-extraction rate associated with turbulent dissipation is typically one to two orders of magnitude smaller than that due to leakage through radiated waves. These analyses are intended only as a quick scale check rather than a precise estimate, both because of the idealized representation of linear drag and the assumption that the solution is unaffected by the inclusion of turbulent dissipation and bottom drag. A more accurate assessment will be presented in the next section using numerical models that account for all of these effects.

5. Comparison with numerical simulations

a. Settings

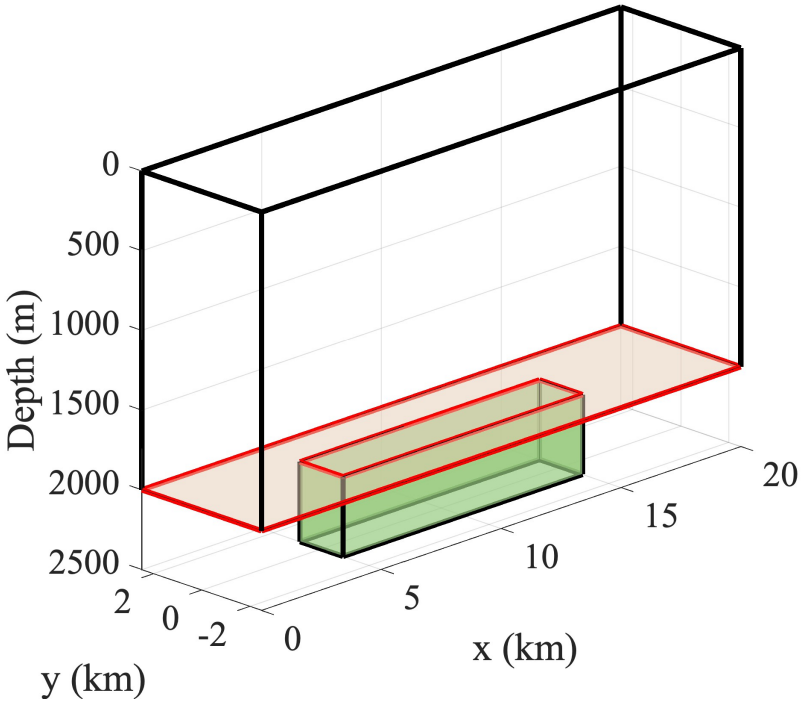

FIG. 5. Simulation domain of the idealized simulation with a box-shaped canyon with $L_z = 500$ m.

In order to test the validity of the theoretical results presented above, we perform hydrostatic numerical simulations using MITgcm in a domain containing a box-shaped canyon at its center, as illustrated in Fig. 5. The domain consists of an open-ocean region with dimensions of 20 km in length, 5 km in width, and H=2000 m in depth. A canyon of dimensions L_x = 10 km and L_y = 1.8 km is carved into the sea floor, with varying depths L_z. This setup precisely replicates the configuration used in our theoretical analysis, enabling a direct comparison between the theoretical predictions and simulation results.

TABLE 1. Summary of Constant Parameters for Simulations

Parameter	Value
Domain size	20 km × 5 km × 3000 m
Canyon size ($L_x \times L_y$)	10 km × 1.8 km
Horizontal resolution	200 m
Vertical resolution	10 m
Grid points ($N_x \times N_y \times N_z$)	$100 \times 25 \times 300$
Stratification (N^2)	$3.92 \times 10^{-6}\,\mathrm{s}^{-2}$
Coriolis parameter (f)	$1 \times 10^{-4}\,\mathrm{s}^{-1}$
Canyon vertical diffusivity/viscosity	$10^{-2}\,\mathrm{m}^2/\mathrm{s}$
Open-ocean vertical diffusivity/viscosity	$10^{-5}\,\mathrm{m}^2/\mathrm{s}$
Tidal forcing amplitude ($\tilde{\eta}_0$)	0.5 m
Tidal forcing period (T)	12 hours
Simulated tidal cycles (n)	20

The system is initialized with a constant stratification of $N^2 = 3.92 \times 10^{-6}\,\mathrm{s}^{-2}$. The Coriolis parameter is set to $f = 1 \times 10^{-4}\,\mathrm{s}^{-1}$. To represent the strong mixing environment observed near the bottom of submarine canyons like the submarine canyon recently measured in the Rockall Trough region (Van Haren et al. 2024), we employ high vertical diffusivity and viscosity values of $\kappa_v = \nu_v = 10^{-2}\,\mathrm{m}^2/\mathrm{s}$ inside the canyon and $\kappa_v = \nu_v = 10^{-5}\,\mathrm{m}^2/\mathrm{s}$ in the open ocean above, respectively. The effects of using smaller vertical diffusivity and viscosity values are discussed in detail in Appendix A. Additionally, Leith hyperviscosity is employed to damp grid-scale noise.

We chose barotropic tides as the forcing because they align well with our theoretical framework and are straightforward to implement numerically. A barotropic tidal forcing with M2 tidal frequency $\omega = 2\pi/T \approx 1.45 \times 10^{-4}\mathrm{s}^{-1}$, wave vector along the x-direction $K_0 = \omega/\sqrt{gH}$ and complex tidal amplitude $\tilde{\eta}_0 = 0.5$ m is implemented in the system by prescribing the tidal velocities u and v of the barotropic tidal solutions at the boundaries. The simulations are run for 10 days, encompassing

20 semidiurnal tidal cycles. Sponge layers are applied at the domain boundaries to prevent the reflection of radiated waves back into the computational domain.

To highlight the system's contrasting responses under near-resonance and off-resonance conditions, we consider two canyon depths: $L_z = 350$ m, which is close to the first-mode resonant depth ($\alpha_c L_x/2 \approx 367$ m), and $L_z = 500$ m, which is off-resonance. For each depth, we compare simulations with no bottom drag to those with quadratic bottom drag, using the stress formulation $\tau = -\rho_0 C_D |\mathbf{u_H}| \mathbf{u_H}$ and $C_D = 2 \times 10^{-3}$. The no-drag configuration is consistent with the assumptions of our theoretical derivation, enabling a direct comparison with idealized predictions. In contrast, simulations with bottom drag provide a more realistic representation of seafloor friction and allow us to distinguish the relative contributions of leakage through the canyon-top interface and bottom friction to the total energy extraction.

TABLE 2. Varying parameters for four simulation cases

Case	L_z (m)	Bottom Drag (C_D)
1	500	No drag ($C_D = 0$)
2	500	Quadratic drag ($C_D = 2 \times 10^{-3}$)
3	350	No drag ($C_D = 0$)
4	350	Quadratic drag ($C_D = 2 \times 10^{-3}$)

b. Amplitude and phase comparisons

The simulation approaches a quasi-steady periodic state after about two tidal cycles, oscillating at the semidiurnal frequency of the external tidal forcing. Because the barotropic flow outside the canyon does not interact with any significant topography (e.g., seamounts, slopes) capable of generating baroclinic waves, there is effectively no baroclinic forcing outside the canyon. This setup provides a clean baseline for comparing our theoretical predictions with numerical results.

Specifically, the theoretical prediction for the along-canyon velocity field is obtained by incorporating the first three odd wave modes (the even modes vanish, as discussed in (13), and higher-order modes have negligible impact on the result). The modal pressure amplitudes are given by (21) and are converted to along-canyon velocity amplitudes using (10) and (13), namely:

$$u_{\text{theory}}(x,z,t) = \text{Re}\left(\hat{u}_{\text{theory}}(x,z)e^{-i\omega t}\right) \simeq \text{Re}\left(\sum_{n=1,3,5} \tilde{A}_{un}\hat{u}_n(x,z)e^{-i\omega t}\right)$$
$$\tilde{A}_{un} = \frac{ik_n}{\omega}\tilde{A}_{pn} \simeq (-iK_0 g\tilde{\eta})\frac{4}{n\pi}\frac{1}{\omega}\frac{i}{\cos(m_n L_z) + iz_n \sin(m_n L_z)}. \tag{29}$$

In the meantime, the tidal component of the along-canyon velocity field at the canyon center can be expressed as

$$u^{\text{tide}}_{\text{sim}}(x, y=0, z, t) \equiv \text{Re}\left[\hat{u}_{\text{sim}}(x,z)\, e^{-i\omega t}\right], \tag{30}$$

where the spatial structure of the complex wave amplitude $\hat{u}_{\text{sim}}(x,z)$ is obtained from a Fourier transform over n tidal periods:

$$\hat{u}_{\text{sim}}(x, y=0, z) = \frac{2}{nT}\int_0^{nT} u_{\text{sim}}(x, y=0, z, t)\, e^{i\omega t}\, dt. \tag{31}$$

Fig. 6 (b,c,e,f) shows the resulting tidal amplitudes $|\hat{u}_{\text{sim}}(x, y=0, z)|$ for simulations with different L_x and with/without bottom drag, and compares them to the theoretical predictions of $|\hat{u}_{\text{theory}}(x,z)|$ in Fig.6 (a,d). Overall, the amplitude patterns agree well with theoretical expectations in the no-drag cases. When bottom drag is included (Fig.6 (c,f)), $|\hat{u}_{\text{sim}}(x, y=0, z)|$ decreases within about 20–30 m of the bottom boundary, but the flow structure farther above remains qualitatively unchanged.

In Fig. 7, we plot the time series of the along-canyon velocity at the bottom center of the canyon $u_{\text{sim}}(x = 5\text{km}, y = 0, z = 0, t)$, where the velocity is largest, and compare it to theoretical predictions of $u_{\text{theory}}(x = 5\text{km}, y = 0, z = 0, t)$ in (29). The theoretical velocities capture the amplitude and phase of the no-drag simulation well in both off-resonance ($L_z = 500$ m) and near-resonance ($L_z = 350$ m) regimes. The near-resonance canyon exhibits a larger velocity amplitude, which is within the expectation. The relative phase of $\tilde{A}_{u1}$ with respect to the complex amplitude of the forcing $-g\eta_x$, given by $-iK_0 g\,\tilde{\eta}\, e^{-i\omega t}$ in the first term of (29), is determined by the last term in (29),

$$\frac{i}{\cos(m_1 L_z) + iz_1 \sin(m_1 L_z)},$$

which we refer to as the phase factor. In the off-resonance case, the cosine term dominates, making the phase factor nearly imaginary; the along-canyon velocity then has a $\pi/2$ phase lag relative to

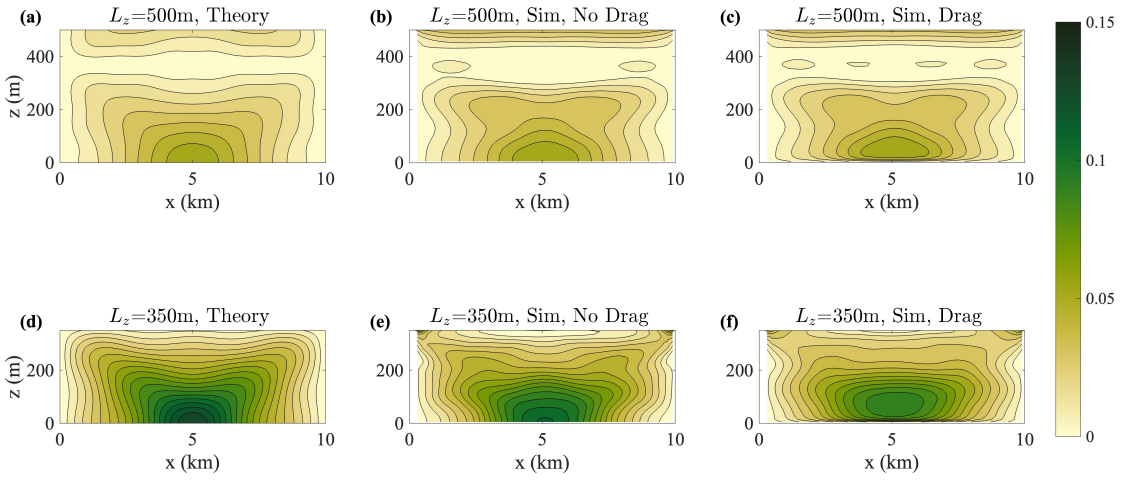

FIG. 6. Comparison of the amplitude of the tidally filtered along-canyon velocity in the along-canyon transect between the theoretical predictions (a, d) and simulations (b, c, e, f), with $L_z = 500$ m and $L_z = 350$ m separately. The contour plots are generated using a uniform interval of 0.0075 m/s.

the forcing. For $L_z = 500$ m, $\cos(m_n L_z) < 0$, and $\tilde{A}_{u1}$ is approximately $\pi/2$ ahead of the forcing. By contrast, in the near-resonance case, the sine term dominates the phase factor, and $\tilde{A}_{u1}$ is nearly in phase with the forcing. Both of these phase relationships are confirmed by our numerical simulations in Fig. 7.

When bottom drag is introduced, the off-resonance phase and amplitude don't change much, whereas in the near-resonance scenario the drag causes a slight amplitude reduction and a small phase shift toward the forcing phase. This behavior is expected because the additional damping reduces the resonance response and shifts the velocity phase closer to that of the forcing. Nonetheless, the canyon's overall dynamics remain dominated by horizontal leakage at the canyon top, as we will further illustrate in the upcoming energy-budget analysis.

c. Energy budget in the simulations

With the above verification of the amplitude and phase of our theoretical predictions, we next examine the energy budget analysis presented in section 4.

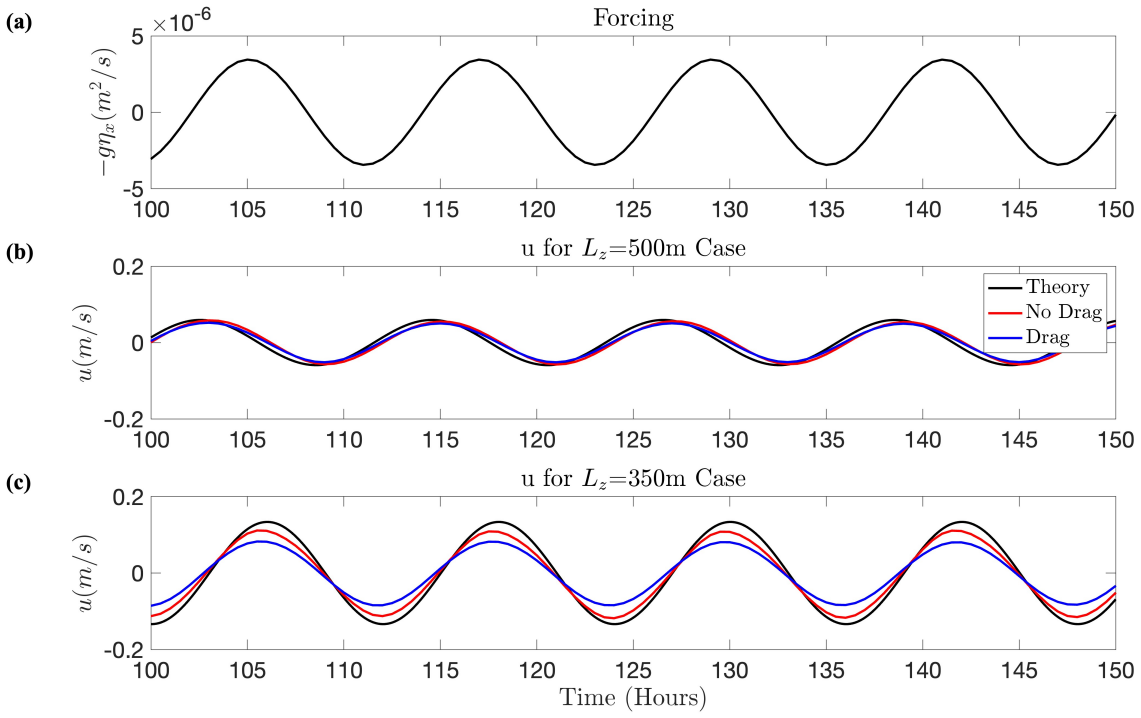

491 FIG. 7. Comparison of the time-dependence of the along-canyon velocity at the bottom-center of the domain
492 between theory and simulations with and without bottom drag for L_z = 500m simulation in (b) and L_z = 350m
493 simulation in (c). The tidal forcing exerted by the barotropic tide from the simulation is plotted in (a) panel for a
494 phase reference.

498 As our simulation is fully three-dimensional, the mean kinetic energy budget for $E_k = \frac{1}{2}\rho_0(u^2+v^2)$
499 in the canyon, averaged over multiple tidal cycles, can be derived from the full Navier–Stokes
500 equations with hydrostatic approximation (1). It can be written as

$$\underbrace{\frac{1}{\rho_0}\overline{\partial_t E_k}^{x,y,z,t}}_{\text{(Tendency)}} = \underbrace{-\frac{1}{L_z}\overline{w\,p_F}^{x,y,t}\Big|_{z=L_z}}_{\text{(Forcing)}} + \underbrace{-\frac{1}{L_z}\overline{w\,p_R}^{x,y,t}\Big|_{z=L_z}}_{\text{(Radiation)}} + \underbrace{\overline{w\,b}^{x,y,z,t}}_{\text{(Buoyancy)}}$$
$$+ \underbrace{-\frac{1}{L_z}\overline{w\,E_k}^{x,y,t}\Big|_{z=L_z}}_{\text{(Advection)}} + \underbrace{\overline{-\epsilon}^{x,y,z,t}}_{\text{(Dissipation)}} + \underbrace{\frac{1}{\rho_0}\frac{1}{L_z}\overline{\boldsymbol{\tau}\cdot\mathbf{u}}^{x,y,t}\Big|_{z=0}}_{\text{(Drag)}}. \tag{32}$$

501 where the six terms represent the following sources and sinks of the kinetic energy: work done
502 by pressure forcing, wave radiation into the open water, buoyancy flux that converts between

potential and kinetic energy, advection of kinetic energy between canyon and open water, turbulent dissipation of kinetic energy and work done by bottom drag. These energy budget terms can be evaluated explicitly in MITgcm from the recorded momentum tendency terms. We performed this processing for both the $L_z = 500$m and $L_z = 350$m simulations with quadratic bottom drag turned on, as shown in Fig. 8.

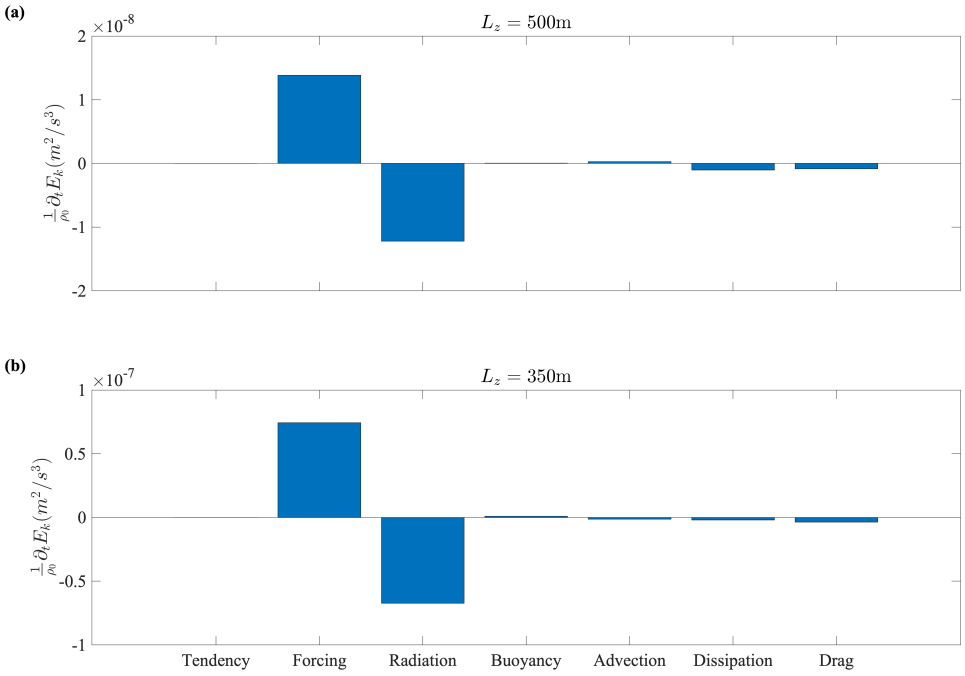

FIG. 8. Energy budget for the volume-mean kinetic energy averaged over 20 tidal cycles, for the off-resonance case $L_z = 500$m and near-resonance case $L_z = 350$m with bottom drag. Note that the scales for the y-axes are different between (a) and (b).

Fig. 8 reveals that the average energy injection is approximately 20 times greater for the near-resonance case than for the off-resonance case. In both scenarios, the dominant energy sink is the leakage term $-\frac{1}{L_z}\overline{w\, p_R}|_{z=L_z}$, which exceeds the bottom drag and turbulent dissipation by more than an order of magnitude, consistent with our earlier discussion in section 4.

6. Extension of the model to a tilted canyon system

In the previous sections, we detailed how standing waves in the canyon can be excited by barotropic tides and low-order baroclinic tides in the open ocean, using the box-canyon model.

In this section, we move one step forward and discuss how these insights can help us understand the canyon with a more realistic shape, for example, those on a continental slope. The connection between a box-canyon model and a tilted canyon model can be understood in Figure 9 (a): the consideration of the arbitrary shape of boundaries and the inclusion of slopes provide two additional levels of complexity. Given these additional complexities, which significantly constrain the tractability of the theoretical framework, we do not attempt a detailed analytical solution here. Instead, we offer a brief outline of the calculation process to highlight the key physical factors that influence the excitation of waves in more realistic canyon geometries.

We extend our canyon model slightly to a configuration shown in Fig. 9(b). We are still assuming that the canyon is narrow compared with the deformation radius, so that we can safely treat it as a 2D wave system. However, we now consider the effect of the continental slope with an angle α and assume this angle doesn't vary too much in the canyon region for simplicity. For the sake of discussion, we rotate the coordinate system at the canyon top interface, aligning the x' coordinate along the tilted interface and the z' coordinate normal to the tilted interface.

The governing tidal excitation process should still be analyzed at the canyon-top interface represented as $z' = z_B$ for simplicity, where the pressure field and the normal velocity to the interface, denoted as $\hat{w}'$, remain continuous. Specifically, the following conditions must be satisfied at the interface:

$$\begin{aligned} \hat{p}_{CA}(x') &= \hat{p}_F(x') + \hat{p}_R(x'), \\ \hat{w}'_{CA}(x') &= \hat{w}'_R(x'), \end{aligned} \tag{33}$$

Here, $\hat{p}_{CA}(x')$ and $\hat{w}'_{CA}(x')$ denote the canyon-wave modes, $\hat{p}_F(x')$ is the pressure field exerted by the low-order waves in the open ocean in the presence of sloped bathymetry, and $\hat{p}_R(x')$ and $\hat{w}'_R(x')$ denote the radiated-wave modes into the open ocean, all evaluated at the canyon-top interface. Similar to our previous arguments, because the forcing waves must satisfy no-normal boundary condition and they typically have wavelengths much larger than the canyon bathymetry scale, $\hat{w}_F(x') \sim 0$.

The procedure for calculating the complex amplitude of the standing waves using boundary condition (33) is similar to what was described in the previous section and reiterated below with a focus on the differences introduced by the consideration of the complicated bathymetry and the slope.

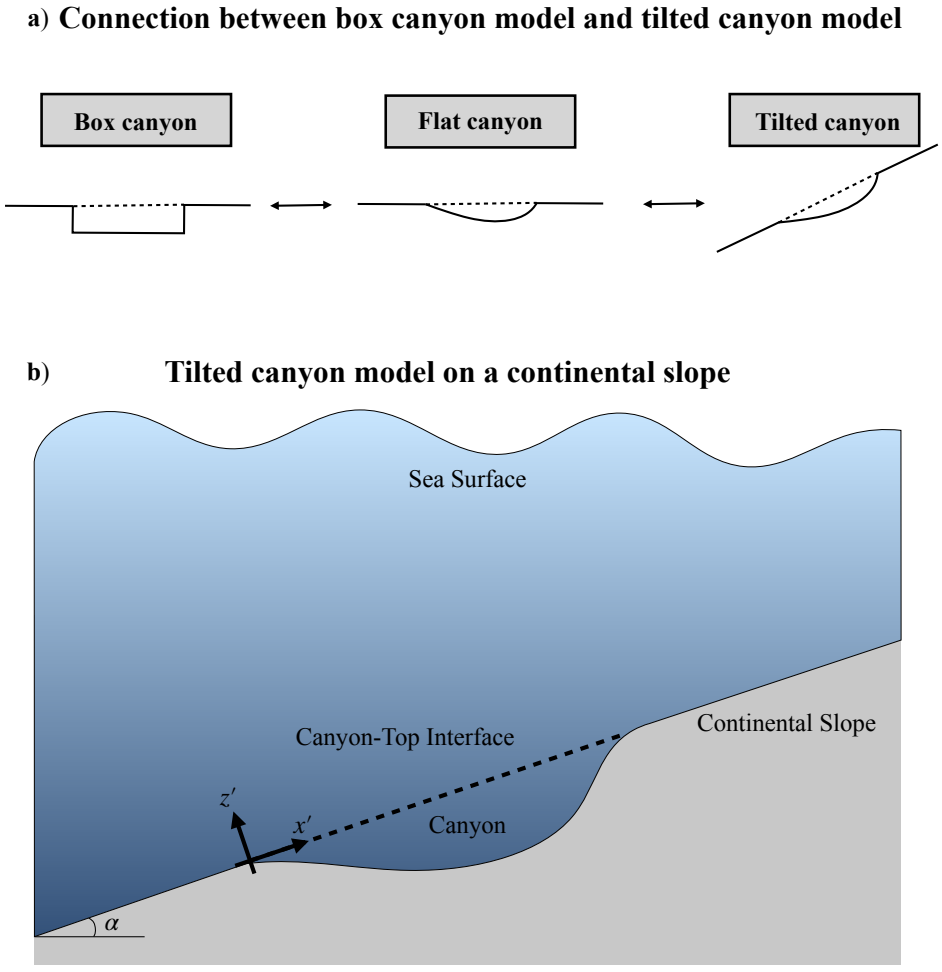

FIG. 9. (a) Schematic illustration demonstrating the extension of the idealized box-canyon model into a more generalized tilted canyon framework. (b) A physically realistic representation of the tilted canyon model situated on a representative continental slope.

Firstly, we need to write down the standing wave modes that can fit into the canyon. These can still be evaluated as the solution of $\hat{\psi}_{xx} - c^2\hat{\psi}_{zz} = 0$, with the boundary condition being $\hat{\psi}$ at the curved solid boundary. It should be mentioned that generally the boundary does not encompass a standing wave solution: if the boundary is everywhere subcritical or supercritical to the Kelvin waves, the Kelvin waves can propagate in the along-canyon direction. However, if the slope along the canyon thalweg experiences a transition from being subcitical to supercritical, then the standing normal modes can be computed by recogonizing the fact $\hat{\psi}_{xx} - c^2\hat{\psi}_{zz} = 0$ has the general solution

of $\hat{\psi} = f(\xi) + g(\eta)$. The normal modes for the standing waves in the canyon can be computed by finding the constraints of f and g functions that satisfy the boundary conditions $\hat{\psi} = 0$ at the solid boundaries. An example of the method for the normal mode calculation process is discussed in the accompanied paper Ma et al. (2025).

Second, the mode is still forced by the tidal motions outside the canyon. Strictly speaking, in the presence of sloped bathymetry there is no sharp separation between barotropic and baroclinic waves. Nevertheless, the most energetic mode outside the canyon is typically the gravest mode that conforms to the sloped bathymetry, which also has longest wavelengths. The pressure of the first several gravest tidal wave fields can be used to estimate $\hat{p}_F(x')$, which can then be decomposed into a summation of canyon pressure modes.

Third, for each mode in the canyon, the relationship between the pressure field of the radiated waves $\hat{p}_R(x')$ can be determined from the normal velocity at the canyon interface, $\hat{w}'_{CY}(x')$. This relation has been explicitly discussed using either a Green's function approach in Grimshaw et al. (1985) or an impedance approach in Appendix B. These radiated waves are qualitatively similar to those excited waves in the idealized canyon considered in this paper or observed in Grimshaw et al. (1985) and effectively leak energies out of narrow canyons.

Finally, one can return to (33), substituting the form of $\hat{p}_R(x')$ into the pressure equation allows for the calculation of the excitation strength of each mode in the canyon, as we have done in the box canyon case.

The detailed analytical solution for wave motion in the general case of a continental slope is complex and beyond the scope of our current study. However, the key insights gained from the box canyon model can be somewhat tested using numerical simulation in this extended setup. Specifically, we performed an additional simulation analogous to that in Section 4, but with a canyon situated on a sloping bathymetry rather than in a flat box configuration. The domain size, resolution, canyon width, and imposed barotropic tidal fluxes at the boundaries remained the same. The one-dimensional bathymetry of the slope and the canyon thalweg are given by: $z_{\text{slope}}(x) = 0.05x - 2000$ and $z_{\text{thalweg}}(x) = 0.05x - 220e^{-(x/4000)^2} - 1950$. Since no direct theoretical prediction was done for this setup, we do not undertake a detailed quantitative analysis. Instead, we highlight that several key insights derived from the box canyon model remain valid here.

In Fig. 10(a,b) we plot the tidal amplitudes of the along-canyon and cross-canyon velocities, respectively, following Eq. (31). As in the box canyon case, the presence of canyon walls strongly suppresses the cross-canyon velocity, while the along-canyon velocity exhibits patterns consistent with standing wave modes. To further illustrate the underlying dynamics, we show in Fig. 10(c) a representative momentum budget for the canyon flow in the x direction, specifically:

$$\underbrace{\overline{u}_t^{z,t}}_{\text{Tendency}} = \underbrace{\overline{-p_x}^{z,t}}_{\text{Pressure Gradient Term}} + \underbrace{f\overline{v}^{z,t}}_{\text{Coriolis Term}} + \underbrace{(-\overline{(uu)_x}^{z,t} - \overline{(uv)_y}^{z,t} - \overline{(uw)_z}^{z,t})}_{\text{Advection Term}} + \underbrace{\overline{(\nu_V u_z)_z}^{z,t} + \overline{(\text{Leith Dissipation})}^{z,t}}_{\text{Diffusion Term}}. \tag{34}$$

Here the $\overline{\cdot}^{z,t}$ represents depth average over the bottom 50 m and time average over 30 minute time intervals taken at an example location of $x = 10$ km in the simulation. The momentum tendency for the along-canyon velocity is dominated by the pressure gradient ($-p_x$), consistent with the dominant balance in Kelvin wave dynamics. Finally, a kinetic energy budget analysis confirms that the main source of energy is the tidal energy input, while radiated energy serves as the primary sink. These results reinforce that our major conclusions from the box canyon scenario also hold when the canyon is embedded in a sloping bathymetry.

In Ma et al. (2025), we conducted realistic simulations to examine the effect of tidal forcing on the topography of a submarine canyon on the continental slope in the Rockall Trough. The wave field patterns observed in our numerical simulations align closely with the lowest mode of standing Kelvin waves in the canyon, confirming that these low-mode standing Kelvin waves are indeed excited as a result of tidal forcing.

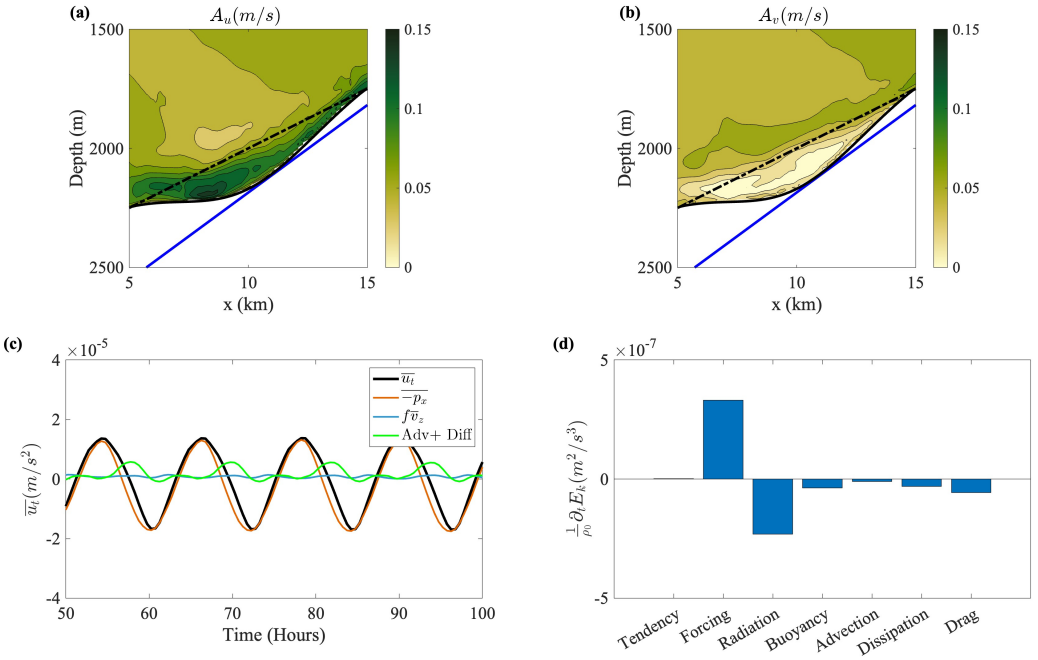

FIG. 10. Analysis of a example tilted-canyon simulation. (a,b) Tidal amplitudes of the along-canyon and cross-canyon velocities. (c) Time series of momentum budget at the x = 10km, following (34) (d): Kinetic energy budget of the titled system.

7. Summary and Conclusions

In this paper, we developed a simple box-canyon model to investigate wave modes in an idealized canyon and to illustrate how these modes are excited by tidal motions outside the canyon. Our analysis demonstrates that the most strongly excited modes in the canyon can be interpreted as standing internal Kelvin waves, whose structure is discretized by the canyon's geometry. These modes couple with external tidal forcing through the interface at the canyon top. By carefully imposing boundary conditions at this interface, we derived theoretical predictions for the spatial patterns, amplitudes, and phases of the internal waves. These predictions agree well with results from idealized numerical simulations of a box-canyon forced by barotropic tides.

This theoretical framework offers a new perspective on the canyon's energy budget. Our analyses, based on both analytical and numerical approaches, show that the dominant balance in the canyon arises between energy input from external barotropic or baroclinic tidal forcing and energy loss via wave radiation into the open ocean at the canyon interfaces. This finding differs from earlier

assumptions, which suggested that bottom drag was the principal energy sink for internal tides in canyons and provides a physical explanation for the tidal resonance effect in the canyon.

We further propose that the key qualitative characteristics from this box-canyon model can be extended to a more complex narrow canyon on geometries like those encountered on the continental slope and ridges, although the calculations become more complex. The core physics remains the same: if there is a transition from subcritical to supercritical slopes (relative to Kelvin wave characteristics) along the canyon thalweg, the standing Kelvin wave system would likely dominate. These modes are excited at the canyon-top interface, where the injected energy is largely balanced by leakage through radiated waves into the open ocean.

These simplified models serve as a foundation for understanding how internal tides are excited, how their spatial patterns and phases are determined, and how energy flows through canyon systems. Real oceanic canyons exhibit far more complex bathymetry. They often meander and may contain terraces, benches, and dendritic structures that can further complicate wave dynamics. Detailed quantification of standing wave structures in such settings will require high-resolution numerical modeling and direct observations from moored instruments, which together can capture the full complexity of internal tide dynamics in submarine canyons.

Finally, we discuss the broader implications of this work for understanding ocean mixing. Our theory suggests that submarine canyons can act as sites of internal tide generation: barotropic tidal forcing at the canyon's upper interface can excite standing waves within the canyon, particularly when the canyon geometry resonates with the tidal forcing. These canyon-confined standing waves have shorter vertical scales, producing stronger shear that may be susceptible to breaking and, in turn, drive mixing. In our setup, we deliberately reduced the magnitude of the tidal forcing to capture the linear regime of wave generation, but for realistic tidal forcings recent literature suggests that the shear associated with the standing wave would go unstable to parameteric instabilities (e.g. Radko 2019; Si et al. 2025).

A practical application of this model is presented in our companion paper Ma et al. (2025), where we demonstrate that the anomalously strong shear observed in the Rockall Trough canyon is driven by standing Kelvin waves. This intensified tidal shear may trigger large-scale, intermittent density overturns, potentially providing a mechanism for the vigorous vertical upwelling documented by Wynne-Cattanach et al. (2024) and further analyzed in the recent work of Naveira Garabato et al.

(2025). Together, these results suggest that similarly strong mixing and upwelling may occur in other canyons with comparable scales and bathymetry capable of supporting standing internal Kelvin waves.

Acknowledgments. This work was supported by the U.S. National Science Foundation (grant OCE-1756264). The simulations presented here were performed using computational resources provided by the National Center for Atmospheric Research (NCAR), sponsored by the National Science Foundation, on the Derecho supercomputer (doi:10.5065/5dfh-8a30). The authors are grateful to Carl Wunsch, Wanying Kang, Glenn R. Flierl, Kurt Polzin, Yidongfang Si, Alberto C. Naveira Garabato, Matthew H. Alford and Shuang Wang for their insightful discussions.

APPENDIX A

Solutions with cross-canyon variations

In the main text, we simplified the analysis by considering only Kelvin wave modes and reducing the system to a two-dimensional framework, neglecting variations in the y-direction. In this appendix, we outline solutions that retain the y-dependence and show that, under the narrow-canyon assumption, the two-dimensional simplification remains valid.

a. Three-dimensional representations of wave modes in the canyon

Incorporating the y-dependence of the modes, the standing wave modes in the canyon can be written as

$$\begin{cases} \hat{p}_{\alpha,0}(x,y,z) = \dfrac{-i\omega}{c}\tilde{A}_0\left[\cos(k_\alpha x)\cosh(\dfrac{fk_\alpha}{\omega}y) - i\sin(k_\alpha x)\sinh(\dfrac{fk_\alpha}{\omega}y)\right]\cos(m_{\alpha,0}z) \\ \hat{u}_{\alpha,0}(x,y,z) = m_{\alpha,0}\tilde{A}_0\left[\sin(k_\alpha x)\cosh(\dfrac{fk_\alpha}{\omega}y) + i\cos(k_\alpha x)\sinh(\dfrac{fk_\alpha}{\omega}y)\right]\cos(m_{\alpha,0}z) \\ \hat{v}_{\alpha,0}(x,y,z) = 0 \\ \hat{w}_{\alpha,0}(x,y,z) = -k_\alpha\tilde{A}_0\left[\cos(k_\alpha x)\cosh(\dfrac{fk_\alpha}{\omega}y) - i\sin(k_\alpha x)\sinh(\dfrac{fk_\alpha}{\omega}y)\right]\sin(m_{\alpha,0}z) \end{cases} \tag{A1}$$

with $\alpha \geqslant 1, \beta = 0$ for Kelvin waves, and

$$
\begin{cases}
\hat{p}_{\alpha,\beta}(x,y,z) = \dfrac{l_\beta \omega(\omega^2 - f^2)}{(l_\beta\omega)^2 + (k_\alpha f)^2}\tilde{A}_0 \\
\qquad\qquad \left[\cos(l_\beta(y+a))\sin(k_\alpha x) + \dfrac{ik_\alpha f}{l_\beta \omega}\sin(l_\beta(y+a))\cos(k_\alpha x)\right]\cos(m_{\alpha,\beta}z) \\
\hat{u}_{\alpha,\beta}(x,y,z) = \dfrac{-f\omega(l_\beta^2 + k_\alpha^2)}{(l_\beta\omega)^2 + (k_\alpha f)^2}\tilde{A}_0 \\
\qquad\qquad \left[\sin(l_\beta(y+a))\sin(k_\alpha x) + \dfrac{ik_\alpha l_\beta}{l_\beta^2 + k_\alpha^2}\dfrac{\omega^2 - f^2}{f\omega}\cos(l_\beta(y+a))\cos(k_\alpha x)\right]\cos(m_{\alpha,\beta}z) \\
\hat{v}_{\alpha,\beta}(x,y,z) = i\tilde{A}_0\sin(l_\beta(y+a))\sin(k_\alpha x)\cos(m_{\alpha,\beta}z) \\
\hat{w}_{\alpha,\beta}(x,y,z) = \dfrac{-i\omega}{N^2}\tilde{A}_0\left[\cos(l_\beta(y+a))\sin(k_\alpha x) + \dfrac{ik_\alpha f}{l_\beta\omega}\sin(l_\beta(y+a))\cos(k_\alpha x)\right]\sin(m_{\alpha,\beta}z)
\end{cases}
\tag{A2}
$$

with $\alpha \geqslant 1$, $\beta \geqslant 1$ for canyon Poincaré waves. Here $k_\alpha \equiv \alpha\pi/L_x$, $l_\beta \equiv \beta\pi/L_y$, $(k_\alpha, m_{\alpha,0})$ follows the Kelvin wave dispersion relation and $(k_\alpha, l_\beta, m_{\alpha,\beta})$ follows the Poincaré wave dispersion relation (discussed in section 2b).

It should be noted that while these wave modes satisfy the boundary condition $\hat{v} = 0$ at $y = \pm L_y/2$, they do not strictly satisfy $\hat{u} = 0$ at the horizontal boundaries $x = 0$ and $x = L_x$. This is evident from the terms proportional to $\cos(k_\alpha x)$ in the expression for $\hat{u}_{\alpha,\beta}$ for both Kelvin and Poincaré waves. However, under the assumption of a narrow canyon ($L_y \ll L_x$), the prefactors of the $\cos(k_\alpha x)$ terms are much smaller than those of the $\sin(k_\alpha x)$ terms, making these functional forms a good approximation to the standing wave fields. Physically, the standing-wave solutions can be interpreted as arising from reflections at $x = 0$ and $x = L_x$, where trapped Poincaré waves are excited in order to enforce the $\hat{u} = 0$ boundary condition (Taylor 1922; Brown 1973). These trapped modes, however, do not influence the interior solutions.

In the main text, we showed that the pressure forcing at the one-dimensional interface above the two-dimensional canyon can be expanded into a complete basis of $\cos(k_n x)$ to excite different modes within the canyon. The orthogonality of the pressure field on the 1D interface continues to hold for the 2D interface. Specifically, the 2D basis functions for the pressure field can be derived directly from (A1) and (A2).

$$\begin{cases} f_{0,0}(x,y) = 1 \\ f_{\alpha\geqslant 1,0}(x,y) = \cos(k_\alpha x)\cosh(\dfrac{fk_\alpha}{\omega}y) - i\sin(k_\alpha x)\sinh(\dfrac{fk_\alpha}{\omega}y) \\ f_{\alpha\geqslant 1,\beta\geqslant 1}(x,y) = \cos(l_\beta(y+\dfrac{L_y}{2}))\sin(k_\alpha x) + \dfrac{ik_\alpha f}{l_\beta\omega}\sin(l_\beta(y+\dfrac{L_y}{2}))\cos(k_\alpha x) \end{cases} \tag{A3}$$

These base functions form complete and orthogonal basis in the domain of $[0, L_x] \times \left[-\frac{L_y}{2}, \frac{L_y}{2}\right]$. Specifically it can be verified that

$$\int_{-a}^{a}\int_{0}^{L_x} f_{\alpha_1,\beta_1}(x,y) f^*_{\alpha_2,\beta_2}(x,y) = 0 \text{ for } \quad (\alpha_1,\beta_1) \neq (\alpha_2,\beta_2) \tag{A4}$$

Therefore, one can expand a 2D pressure forcing field into these base functions to determine the forcing coefficient $\tilde{C}_{\alpha,\beta}$ of each mode:

$$\hat{p}_F(x,y) \equiv \hat{p}_F(x,y,L_z) = \sum_{\alpha,\beta} \tilde{C}_{p\alpha,\beta} f_{\alpha,\beta}(x,y) \tag{A5}$$

Similar with our discussions in the main text, the wave model (α,β) that has the higher $|\tilde{C}_{p\alpha,\beta}|$ would feel the forcing more strongly.

We can again get a better sense of the coupling strength for the long-wave forcing if we take make the Taylor expansion:

$$\hat{p}^F(x,y) \approx \hat{p}^F_{x0}x + \hat{p}^F_{y0}y + \hat{p}^F_0 \tag{A6}$$

The forcing coefficient of the 3D Kelvin wave field can be calculated by expanding 2D function $f(x,y) = x$ and $f(x,y) = y$ into the base functions $f_{\alpha,\beta}(x,y)$. It can be shown, in this case, the forcing coefficient of the 3D Kelvin wave field takes the following form:

$$\begin{aligned} \tilde{C}_{\alpha,0} &= -\hat{p}^F_{x0}\frac{4L_x}{\alpha^2\pi^2}\frac{1}{\cosh(fk_\alpha L_y/2\omega)} \\ &\quad - \hat{p}^F_{y0}\frac{4L_x i}{\alpha^2\pi^2}\frac{\omega}{f}\left[\frac{fk_\alpha L_y/2\omega}{\sinh(fk_\alpha L_y/2\omega)} - \frac{1}{\cosh(fk_\alpha L_y/2\omega))}\right] \\ &\approx -\hat{p}^F_{x0}\frac{4L_x}{\alpha^2\pi^2} + O((\frac{fk_\alpha L_y}{2\omega})^2), \quad \text{when } \alpha \text{ is odd} \end{aligned} \tag{A7}$$

These calculations from the three-dimensional formulae provide a more accurate forcing coefficient for the Kelvin wave modes with mode number α. However, it can be seem that as long as we are sticking to the low wave number α which has $k_\alpha L_y << 1$, the calculation based on the 2D picture provide a fairly good approximation for forcing coefficient. Specifically, the pressure gradient in the y direction only weakly coupled with the Kelvin wave modes in the canyon and can be reasonably ignored in our discussion of 2D picture in the main text.

b. The attenuation of canyon Poincaré wave modes by turbulence

Besides the Kelvin wave modes discussed in the main text, the canyon Poincaré wave modes can also be excited in our box-canyon model. However, accounting for the excitation of Poincaré wave modes significantly complicates the problem. Fortunately, our idealized simulations reveal that these Poincaré wave modes are attenuated when viscosity and diffusivity are increased to capture elevated turbulent activity, while Kelvin wave modes remain relatively unaffected by turbulent dissipation. This difference arises because the vertical wavenumber of Poincaré waves is much larger than that of Kelvin waves, making them more susceptible to dissipation.

To illustrate this, we compare two runs of the idealized simulation, both simulating the canyon wave fields under barotropic forcing alone. These simulations share the same setup but differ in diffusivity and viscosity values in the canyon, with $\kappa = \nu = 10^{-4}\,\mathrm{m}^2/\mathrm{s}$ and $\kappa = \nu = 10^{-2}\,\mathrm{m}^2/\mathrm{s}$, respectively. The attenuation of the canyon Poincaré wave modes under higher diffusivity and viscosity is evident from two perspectives.

First, the tidally-filtered magnitude of the cross-canyon velocity is compared, as shown in Fig. A1(a). The cross-canyon velocity, represented by the high-m modes, is strongly dissipated when $\kappa = \nu = 10^{-2}\,\mathrm{m}^2/\mathrm{s}$. Since Kelvin wave modes do not contribute to the cross-canyon velocity, this reduction in amplitude reflects the attenuation of the Poincaré wave modes.

Second, a more quantitative analysis can be performed by examining the discretized spectrum of kinetic energy at the tidal frequency. This is achieved using a discrete cosine transform in the z-direction combined with a discrete sine transform in the x-direction, applied to the tidally filtered u and v velocity fields at each y-slice. The kinetic energy for each mode is averaged over the y-direction and shown in Fig. A1(c,d). The dispersion relations for the Kelvin wave modes and the mode-1 ($\beta = 1$) Poincaré wave modes are also plotted for reference.

In Fig. A1(c), under low turbulence levels, the wave kinetic energy is dominated by the lowest-order Kelvin wave modes ($\alpha = 1, 3, 5$) and the Poincaré wave modes $(\alpha, \beta) = (1,1), (3,1), (5,1)$. The most energetic modes are the $(\alpha, \beta) = (1, 0)$ Kelvin wave mode and the $(\alpha, \beta) = (1, 1)$ Poincaré wave modes. The excitation of only odd-numbered modes aligns with our theoretical predictions. In Fig. A1(d), where κ and ν are increased to $10^{-2}\,\mathrm{m}^2/\mathrm{s}$, the energy of the $(\alpha, \beta) = (1, 3)$ and $(1, 5)$ Poincaré wave modes is significantly attenuated, while the energy of the $(\alpha, \beta) = (1, 1)$ mode is spread, consistent with the observations in Fig. A1(b). Thus, ignoring the contributions of Poincaré wave modes becomes a better approximation in high-turbulence environments.

For example, in the BLT canyon that is susceptible to strong convective mixing event within the focus of study of Ma et al. (2025), mean turbulent diapycnal diffusivity are estimated from the measured thermal variance dissipation to be on the order of $10^{-2}\,\mathrm{m}^2/\mathrm{s}$ (Van Haren et al. (2024)). Additionally, the turbulent diffusivities in the realistic simulation Ma et al. (2025) reach this same order of magnitude, as dictated by the implemented turbulent closure. Consequently, high-vertical-wavenumber Poincaré wave modes are absent in both observational data and our realistic simulations.

APPENDIX B

Effective impedance for the waves radiated into the open ocean

In this Appendix, we discussed the derivation of the impedance form (18) shown in the main text.

We start by writing the radiated wave field as, following (A1):

$$\begin{aligned} \hat{w}_R(x, y, z \geqslant L_z) &= \int_{-\infty}^{\infty} \int_{-\infty}^{\infty} \hat{w}_R(k, l)\, e^{i(kx+ly+m(z-L_z))}\, dk\, dl, \\ \hat{p}_R(x, y, z \geqslant L_z) &= \int_{-\infty}^{\infty} \int_{-\infty}^{\infty} Z(k, l)\, \hat{w}_R(k, l)\, e^{i(kx+ly+m(z-L_z))}\, dk\, dl, \end{aligned} \tag{B1}$$

The wave amplitude in the continuum $\hat{w}_R(k, l)$ can be determined by the Fourier transform:

$$\hat{w}_R(k, l) = \mathcal{F}\left[\hat{w}_R(x, y, z = L_z)\right] \equiv \left(\frac{1}{2\pi}\right)^2 \int_0^{L_x} \int_{-L_y/2}^{L_y/2} \hat{w}_R(x, y, z = L_z) e^{-ikx-ily} dx dy \tag{B2}$$

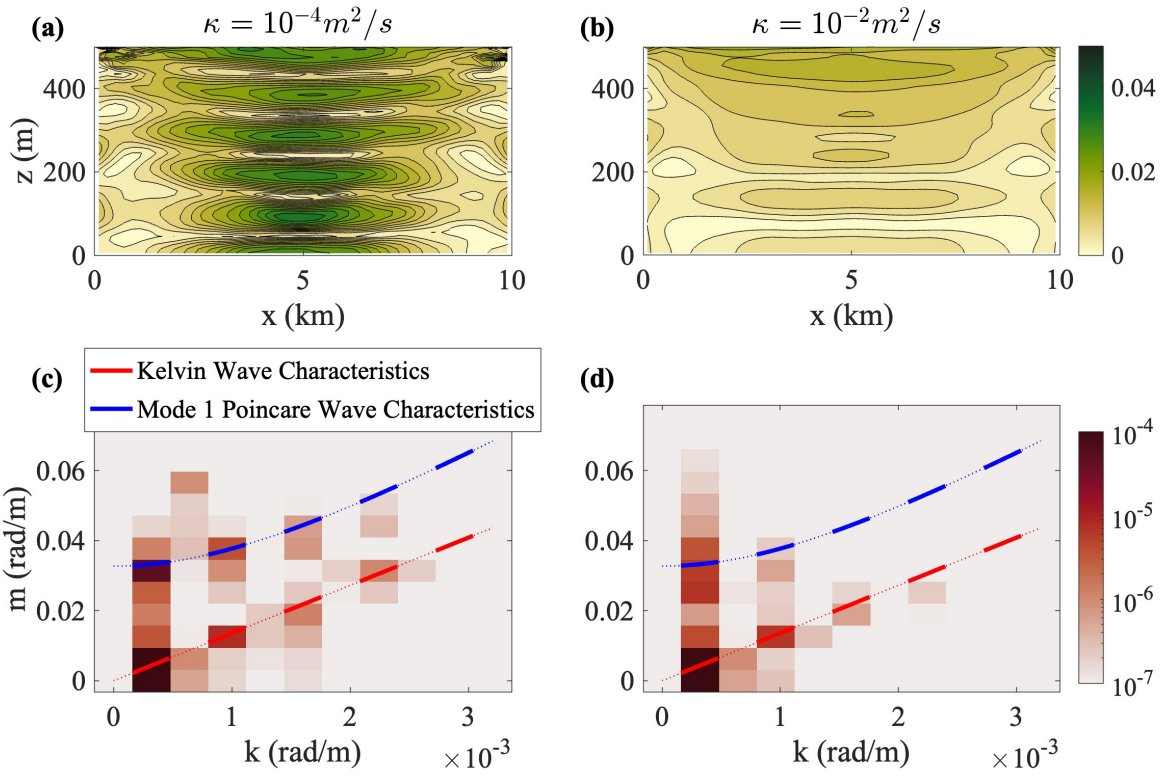

FIG. A1. (a,b): Tidally-filtered magnitude of the cross-canyon velocity v for idealized simulations with $\nu = \kappa = 10^{-4}\,\mathrm{m}^2/\mathrm{s}$ and $\nu = \kappa = 10^{-2}\,\mathrm{m}^2/\mathrm{s}$, respectively. (c,d): Spectral density of kinetic energy in the (k, m) plane for the two simulations using the discrete cosine transformation, respectively. The Kelvin wave and Poincaré wave characteristics are shown as red and blue curves, respectively. Only solid lines for odd modes, which are coupled with the barotropic tidal forcing, are displayed.

therefore, the pressure field at the canyon-top interface can be simplified as:

$$\begin{aligned} \hat{p}_R(x, y, z = L_z) &= \int_{-\infty}^{\infty} \int_{-\infty}^{\infty} Z(k, l) \mathcal{F}\left[\hat{w}_R(x, y, z = L_z)\right] e^{ikx + ily} dk dl \\ &\equiv \mathcal{F}^{-1}\left[Z(k, l) \mathcal{F}\left[\hat{w}_R(x, y, z = L_z)\right]\right] \end{aligned} \tag{B3}$$

This relation shows us that the radiated pressure field at the canyon-top interface $\hat{p}_R(x, y, z = L_z)$ can be linearly determined by the radiated vertical velocity field $\hat{w}_R(x, y, z = L_z)$.

We have shown in Appendix A that the base functions $p_{\alpha,\beta}(x,y)$ form a complete and orthogonal basis, therefore, we can decompose the pressure field at the interface $\hat{p}_R(x,y,z=L_z)$. This allows us to decompose the radiated field into the discrete modes:

$$\begin{aligned}\hat{p}_R(x,y,z=L_z) &= \sum_{\alpha,\beta} \tilde{B}_{p\alpha,\beta} f_{\alpha,\beta}(x,y) \\ \hat{w}_R(x,y,z=L_z) &= \sum_{\alpha,\beta} \tilde{B}_{w\alpha,\beta} f_{\alpha,\beta}(x,y)\end{aligned} \tag{B4}$$

Take (B4) into (B3) we would have a linear relation between each modes, namely:

$$\tilde{B}_{p\alpha,\beta} = \sum_{\alpha,\beta,\alpha',\beta'} Z_{\alpha,\beta,\alpha',\beta'} \tilde{B}_{w\alpha,\beta} \tag{B5}$$

where $Z_{\alpha,\beta,\alpha',\beta'}$ is the effective impedance tensor for radiated waves at the canyon-top interface, whose value can be determined through:

$$Z_{\alpha,\beta,\alpha',\beta'} = \frac{\int_{-a}^{a}\int_{0}^{L_x} f^*_{\alpha,\beta}(x,y)\mathcal{F}^{-1}\left[Z(k,l)\mathcal{F}\left[f_{\alpha',\beta'}(x',y')\right]\right]dxdy}{\sqrt{\int_{-a}^{a}\int_{0}^{L_x}|f_{\alpha,\beta}(x,y)|^2dxdy}\sqrt{\int_{-a}^{a}\int_{0}^{L_x}|f_{\alpha',\beta'}(x,y)|^2dxdy}} \tag{B6}$$

The accurate analytical solution for the effective impedance tensor is hard to be obtained, rather it can be evaluated numerically.

The fact that this is a tensor indicates that the radiated waves can mix different wave modes. However, numerical evaluation of the tensor matrix reveals that it is predominantly governed by its diagonal elements. In fact, the most rigorous calculation would necessarily take the matrix form by considering the interaction of all the modes, however, the introduction of these non-diagonal terms would only lead to minor differences and therefore they are ignored for simplicity. This is essentially the same as the "Plane-wave approximation" made in the early investigation of Grimshaw et al. (1985).

By focusing only on the diagonal elements, we can greatly simplify the system, reducing (B5) to the single relation:

$$\tilde{B}_{p\alpha,\beta} \approx Z_{\alpha,\beta,\alpha,\beta}\tilde{B}_{w\alpha,\beta}, \tag{B7}$$

where the simplification captures the dominant contributions while neglecting off-diagonal interactions. For the Kelvin wave modes, which is the dominating mode in the canyon. This becomes:

$$\tilde{B}_{p\alpha,0} \approx Z_{\alpha,0,\alpha,0}\tilde{B}_{w\alpha,0}, \quad \text{or} \quad \tilde{B}_{pn} \approx Z(k_n)\tilde{B}_{wn} \quad \text{using the notation of the maintext.} \tag{B8}$$

and the effective impedance ratio $Z_R(k_n)$, can be then derived as:

$$Z_R = \frac{N}{k_n}\frac{\sqrt{\omega^2 - f^2}}{\omega}\frac{\int_{-L_y/2}^{L_y/2}\int_0^{L_x} f^*_{n,0}(x,y)\mathcal{F}^{-1}\left[\frac{k_n}{\sqrt{k^2+l^2}}\mathcal{F}\left[f_{n,0}(x',y')\right]\right]dxdy}{\int_{-L_y/2}^{L_y/2}\int_0^{L_x}|f_{\alpha,0}(x,y)|^2 dxdy} \tag{B9}$$

Under the limit of $L_y \ll L_x$, we would have $k_n L_y \sim n\pi L_y/L_x \ll 1$ for the low modes (e.g., $n = 1, 3, 5$) and therefore, we have

$$\begin{aligned} f_{n,0}(x,y) &= \cos(k_n x)\cosh(\frac{f k_n}{\omega}y) - i\sin(k_n x)\sinh(\frac{f k_n}{\omega}y) \\ &\approx \cos(k_n x) \end{aligned} \tag{B10}$$

Effectively, equation (B6) can be regarded as the average impedance over all possible modes in the k, l space. Since $L_y \ll L_x$, the cross-canyon wavenumbers l for the radiated wave fields are generally much larger than the along-canyon wavenumber and dominate the impedance. As a result, the spectrum spread in the k direction effectively does not matter for the averaging process. In other words, we can approximate k as k_n, simplifying the 2D integration to a 1D integration,

which can be written as:

$$
\begin{aligned}
Z_R(k_n)/(\frac{N}{k_n}) &\approx \frac{\sqrt{\omega^2-f^2}}{\omega}\frac{\int_{-\frac{L_y}{2}}^{\frac{L_y}{2}}\mathcal{F}_{1D}^{-1}[\frac{k_n}{\sqrt{k^2+l^2}}\mathcal{F}_{1D}\left[\chi_{[-\frac{L_y}{2},\frac{L_y}{2}]}(y')\right]dy}{\int_{-\frac{L_y}{2}}^{\frac{L_y}{2}}1dy} \\
&= \frac{\sqrt{\omega^2-f^2}}{\omega}\frac{1}{2\pi}\frac{1}{L_y}\int_{-\infty}^{\infty}[\int_{-\frac{L_y}{2}}^{\frac{L_y}{2}}e^{ily}dy][\int_{-\frac{L_y}{2}}^{\frac{L_y}{2}}e^{-ily'}dy']\frac{k_n}{\sqrt{k^2+l^2}}dl \\
&= \frac{\sqrt{\omega^2-f^2}}{\omega}\frac{1}{2\pi}\frac{1}{L_y}\int_{-\infty}^{\infty}\frac{4\sin^2(al)}{l^2}\frac{k}{\sqrt{k^2+l^2}}dl \\
&= \frac{\sqrt{\omega^2-f^2}}{\omega}\frac{1}{2\pi}G_{2,4}^{2,2}\left((\frac{kL_y}{2})^2\middle|\begin{matrix}\frac{1}{2},1\\ \frac{1}{2},\frac{1}{2},-\frac{1}{2},0\end{matrix}\right) \\
&= \frac{\sqrt{\omega^2-f^2}}{\omega}\frac{1}{2\pi}\left[-(k_nL_y)\ln(k_nL_y)+(3-2\gamma+\ln 2)k_nL_y+O((k_nL_y)^3\ln(k_nL_y))\right] \\
&\text{when } k_nL_y << 1
\end{aligned}
\tag{B11}
$$

where $\mathcal{F}_{1D}$ represents the 1D Fourier transform in the y direction, and $\chi_{[-\frac{L_y}{2},\frac{L_y}{2}]}(y')$ is the window function, which is 1 within the interval $[-\frac{L_y}{2},\frac{L_y}{2}]$ and 0 elsewhere. Here

$$
G_{2,4}^{2,2}\left(x\middle|\begin{matrix}\frac{1}{2},1\\ \frac{1}{2},\frac{1}{2},-\frac{1}{2},0\end{matrix}\right) \tag{B12}
$$

is a Meijer G-function with upper parameters $\frac{1}{2}$ and 1, lower parameters $\frac{1}{2},\frac{1}{2},-\frac{1}{2}$, and 0, and argument $\frac{kL_y}{2}$. It is a generalized special function used to represent complex mathematical expressions, whose dominant term for the Taylor expansion is $-2x^{1/2}\ln x+(6-4\gamma)x^{1/2}+O(x^3\ln x)$ at $x=0$ and used in the above derivation. Here, $\gamma\approx 0.57721$ is the Euler–Mascheroni constant.

Finally, it should be noted that in Grimshaw et al. (1985), a closely related quantity, namely reflectivity r, is discussed. Reflectivity is defined as the ratio of pressure perturbation between the incoming Kelvin wave and the reflected wave in the context of an infinitely deep canyon. The reflectivity defined in that context is related to the impedance ratio here as $r=(1-z_n)/(1+z_n)$. However, reflectivity is not employed in our theory because the waves in the canyon are standing waves rather than propagating waves.

References

Alberty, M., S. Billheimer, M. Hamann, C. Ou, V. Tamsitt, A. Lucas, and M. Alford, 2017: A reflecting, steepening, and breaking internal tide in a submarine canyon. *Journal of Geophysical Research: Oceans*, **122 (8)**, 6872–6882.

Alford, M. H., and P. MacCready, 2014: Flow and mixing in juan de fuca canyon, washington. *Geophysical Research Letters*, **41 (5)**, 1608–1615.

Alford, M. H., and Coauthors, 2025: Buoyancy flux and mixing efficiency from direct, near-bottom turbulence measurements in a submarine canyon. *Journal of Physical Oceanography*, **55 (2)**, 97–118.

Allen, S., and X. Durrieu de Madron, 2009: A review of the role of submarine canyons in deep-ocean exchange with the shelf. *Ocean Science*, **5 (4)**, 607–620.

Aslam, T., R. A. Hall, and S. R. Dye, 2018: Internal tides in a dendritic submarine canyon. *Progress in Oceanography*, **169**, 20–32.

Baines, P. G., 1983: Tidal motion in submarine canyons—a laboratory experiment. *Journal of Physical Oceanography*, **13 (2)**, 310–328.

Brown, P., 1973: Kelvin-wave reflection in a semi-infinite canal.

Garabato, A. N., and Coauthors, 2025: Convective turbulent mixing drives rapid upwelling along the ocean's bottom boundary, unpublished manuscript. *submitted to Science Advances*.

Gill, A. E., 2016: *Atmosphere—ocean dynamics*. Elsevier.

Gordon, R., and N. Marshall, 1976: Submarine canyons: Internal wave traps? *Geophysical Research Letters*, **3 (10)**, 622–624.

Grimshaw, R., P. Baines, and R. Bell, 1985: The reflection and diffraction of internal waves from the junction of a slit and a half-space, with application to submarine canyons. *Dynamics of atmospheres and oceans*, **9 (2)**, 85–120.

Hall, R. A., T. Aslam, and V. A. Huvenne, 2017: Partly standing internal tides in a dendritic submarine canyon observed by an ocean glider. *Deep Sea Research Part I: Oceanographic Research Papers*, **126**, 73–84.

Hall, R. A., and G. S. Carter, 2011: Internal tides in monterey submarine canyon. *Journal of Physical Oceanography*, **41 (1)**, 186–204.

Hamann, M. M., M. H. Alford, A. J. Lucas, A. F. Waterhouse, and G. Voet, 2021: Turbulence driven by reflected internal tides in a supercritical submarine canyon. *Journal of Physical Oceanography*, **51 (2)**, 591–609.

Harris, P. T., and T. Whiteway, 2011: Global distribution of large submarine canyons: Geomorphic differences between active and passive continental margins. *Marine Geology*, **285 (1-4)**, 69–86.

Hotchkiss, F. S., and C. Wunsch, 1982: Internal waves in hudson canyon with possible geological implications. *Deep Sea Research Part A. Oceanographic Research Papers*, **29 (4)**, 415–442.

Kunze, E., 2017: Internal-wave-driven mixing: Global geography and budgets. *Journal of Physical Oceanography*, **47 (6)**, 1325–1345.

Kunze, E., L. K. Rosenfeld, G. S. Carter, and M. C. Gregg, 2002: Internal waves in monterey submarine canyon. *Journal of physical oceanography*, **32 (6)**, 1890–1913.

Le Souëf, K. E., and S. Allen, 2014: Physical modeling of tidal resonance in a submarine canyon. *Journal of Geophysical Research: Oceans*, **119 (2)**, 1324–1343.

Ma, Y., R. Ferrari, K. Polzin, M. H. Alford, A. C. N. Garabato, and G. Voet, 2025: Standing wave-induced tidal shear in a submarine canyon in the rockall trough.

Masunaga, E., M. H. Alford, A. J. Lucas, and A. R.-M. Freudmann, 2023: Numerical simulations of internal tide dynamics in a steep submarine canyon. *Journal of Physical Oceanography*, **53 (11)**, 2669–2686.

Naveira Garabato, A. C., and Coauthors, 2025: Connecting mixing to upwelling along the ocean's sloping boundary. *Geophysical Research Letters*, **52 (22)**, e2025GL119 186.

Petruncio, E. T., L. K. Rosenfeld, and J. D. Paduan, 1998: Observations of the internal tide in monterey canyon. *Journal of Physical Oceanography*, **28 (10)**, 1873–1903.

Radko, T., 2019: Instabilities of a time-dependent shear flow. *Journal of Physical Oceanography*, **49 (9)**, 2377–2392.

Rhines, P., 1970: Edge-, bottom-, and rossby waves in a rotating stratified fluid. *Geophysical and Astrophysical Fluid Dynamics*, **1 (3-4)**, 273–302.

Si, Y., R. Ferrari, and G. Voet, 2025: Tidally induced turbulence in the abyssal ocean. *arXiv preprint arXiv:2509.05869*.

Sutherland, G., C. Garrett, and M. Foreman, 2005: Tidal resonance in juan de fuca strait and the strait of georgia. *Journal of Physical Oceanography*, **35 (7)**, 1279–1286.

Swart, N., S. E. Allen, and B. Greenan, 2011: Resonant amplification of subinertial tides in a submarine canyon. *Journal of Geophysical Research: Oceans*, **116 (C9)**.

Taylor, G. I., 1922: Tidal oscillations in gulfs and rectangular basins. *Proceedings of the London Mathematical society*, **2 (1)**, 148–181.

Van Haren, H., G. Voet, M. H. Alford, B. Fernández-Castro, A. C. N. Garabato, B. L. Wynne-Cattanach, H. Mercier, and M.-J. Messias, 2024: Near-slope turbulence in a rockall canyon. *Deep Sea Research Part I: Oceanographic Research Papers*, **206**, 104 277.

Wain, D., M. Gregg, M. Alford, R.-C. Lien, R. Hall, and G. Carter, 2013: Propagation and dissipation of the internal tide in upper monterey canyon. *Journal of geophysical research: Oceans*, **118 (10)**, 4855–4877.

Waterhouse, A. F., J. A. Mackinnon, R. C. Musgrave, S. M. Kelly, A. Pickering, and J. Nash, 2017: Internal tide convergence and mixing in a submarine canyon. *Journal of Physical Oceanography*, **47 (2)**, 303–322.

Wynne-Cattanach, B. L., and Coauthors, 2024: Observations of diapycnal upwelling within a sloping submarine canyon. *Nature*, **630 (8018)**, 884–890.

Zhang, W. G., T. F. Duda, and I. A. Udovydchenkov, 2014: Modeling and analysis of internal-tide generation and beamlike onshore propagation in the vicinity of shelfbreak canyons. *Journal of physical oceanography*, **44 (3)**, 834–849.

Zhao, Z., M. H. Alford, J. B. Girton, L. Rainville, and H. L. Simmons, 2016: Global observations of open-ocean mode-1 m 2 internal tides. *Journal of Physical Oceanography*, **46 (6)**, 1657–1684.

Zhao, Z., M. H. Alford, R.-C. Lien, M. C. Gregg, and G. S. Carter, 2012: Internal tides and mixing in a submarine canyon with time-varying stratification. *Journal of Physical Oceanography*, **42 (12)**, 2121–2142.